

## Reduced-order modeling for complex 3D seismic wave propagation

John M. Rekoske<sup>1</sup>, Dave A. May<sup>1</sup>, Alice-Agnes Gabriel<sup>1,2</sup>

<sup>1</sup>Scripps Institution of Oceanography, University of California, San Diego, 9500 Gilman Drive, La Jolla, CA, USA

<sup>2</sup>Department of Earth and Environmental Sciences, Ludwig-Maximilians-Universität München, Munich, Germany

### Summary

Elastodynamic Green's functions are an essential ingredient in seismology as they form the connection between direct observations of seismic waves and the earthquake source. They are also fundamental to various seismological techniques including physics-based ground motion prediction and kinematic or dynamic source inversions. In regions with established 3D models of the Earth's elastic structure, such as southern California, 3D Green's functions can be computed using numerical simulations of seismic wave propagation. However, such simulations are computationally expensive which poses challenges for real-time ground motion prediction and uncertainty quantification in source inversions. In this study, we address these challenges by using a reduced-order model (ROM) approach that enables the rapid evaluation of approximate Green's functions. The ROM technique developed approximates three-component time-dependent surface velocity wavefields obtained from numerical simulations of seismic wave propagation of an arbitrary moment tensor source. We apply our ROM approach to a 50 km  $\times$  40 km area in the greater Los Angeles area accounting for topography, site effects, 3D subsurface velocity structure, and viscoelastic attenuation. The ROM constructed for this region enables rapid computation (0.001 CPU hours) of complete, high-resolution (500 m spacing), 0.5 Hz surface velocity wavefields that are accurate for a shortest wavelength of 1.0 km for a single moment tensor source. Using leave-one-out cross validation, we measure the accuracy of our Green's functions for the CVM-S velocity model in both the time-domain and frequency-domain. Averaged across all sources, receivers, and time steps, the error in the rapid seismograms is less than 0.01 cm/s. We demonstrate that the ROM can accurately and rapidly reproduce simulated seismograms for generalized moment tensor sources in our region, as well as kinematic sources by using a finite fault model of the 1987  $M_W$  5.9 Whittier Narrows earthquake as an example. We envision that our rapid, approximate Green's functions will be useful for constructing rapid ground motion synthetics with high spatial resolution, and to improve the uncertainty quantification in earthquake source inversions.

### Keywords

Machine learning; computational seismology; earthquake ground motions; wave propagation.

# 1 Introduction

Elastodynamic Green’s functions are essential tools that seismologists use to predict ground motions from future earthquakes. They are also an important ingredient for solving inverse problems to understand the earthquake source, assuming a seismic velocity model describing the Earth’s structure. Mathematically, the Green’s function, sometimes described in terms of the strain Green’s tensor (SGT), represents the seismic impulse response of a medium (e.g., [Zhao et al., 2006](#)). It characterizes the entire wave propagation effects between a source location and a receiver location ([Aki & Richards, 2002](#)). One approach to obtain Green’s functions is to derive empirical Green’s functions (EGFs) from real seismograms that record seismic events sufficiently similar in location and mechanism to the analyzed earthquake. However, this approach requires that suitable repeated events have occurred in the area of interest (e.g., [Hough, 1998](#); [Hartzell, 1978](#); [Abercrombie, 2015](#); [Hough, 1997](#); [Yang et al., 2020](#)). Once obtained, EGFs can be used to accurately simulate ground motions for future events or to invert for earthquake source parameters (e.g., [Dreger, 1994](#); [Liu & Archuleta, 2004](#)). In contrast to EGFs, theoretical Green’s functions can be calculated by assuming a (simple) seismic velocity model that describes the Earth’s structure. Theoretical (analytically and numerically derived) Green’s functions can be rapidly calculated for Earth models assuming a 1D or axisymmetric structure, where the seismic velocities vary only with depth, such as through InstaSeis ([van Driel et al., 2015](#); [Nissen-Meyer et al., 2014](#)). However, once lateral variations in the Earth’s structure, or topography, are introduced, there exist no analytical solutions, and numerical simulations to compute Green’s functions become computationally more demanding. Modern crustal seismic velocity models often contain significant lateral changes in velocity, such as velocity models describing southern California basins (e.g., [Shaw et al., 2015](#); [Magistrale et al., 2000](#); [Lin et al., 2007](#); [Li et al., 2023b](#)) or subduction zone settings (e.g., [Koketsu et al., 2008](#); [Fujiwara et al., 2009](#); [Stephenson et al., 2017](#)). In such models, 3D Green’s functions can deviate from the ones derived from 1D reference models due to basin amplification and site effects (e.g., [Moschetti et al., 2024, 2021](#); [Rekoske et al., 2022](#); [Frankel et al., 2009](#); [Olsen, 2000](#)). Accounting for these effects is crucial for accurate ground motion prediction and the resulting seismic hazard estimates.

Numerical simulations of seismic wave propagation remain computationally expensive and impractical for real-time problems despite substantial progress in the underlying numerical methods (e.g., [Komatitsch & Vilotte, 1998](#); [Komatitsch & Tromp, 1999](#); [van Driel et al., 2020](#); [Cui et al., 2010](#); [Rodgers et al., 2018](#); [Heinecke et al., 2014](#)) and increasing computing power. Reaching regional-scale, high-frequency simulations which are necessary for ground motion modeling and probabilistic seismic hazard assessment can require up to  $10^3 - 10^4$  CPUh on the world’s most powerful supercomputers for just a single earthquake (e.g., [Rodgers et al., 2020](#); [Hu et al., 2022](#); [Taufiqurrahman et al., 2022](#); [Graves et al., 2011](#)). This computational expense challenges applications in real-time and near-real-time seismology. Rapid efforts to constrain finite fault models in real-time (e.g., [Böse et al., 2012, 2018](#); [Crowell et al., 2012](#); [Minson et al., 2014](#); [Murray et al., 2022](#)) for earthquake early warning and to produce shake maps ([Worden & Wald, 2016](#)) could be improved by using 3D Green’s functions that account for lateral changes in seismic velocities or attenuation. Additionally,

more detailed rupture models could be used to rapidly constrain the ground motion levels by using physics-informed estimates for the inferred slip distribution, compared to empirical ground motion models (GMMs) which average across many earthquake sources (e.g., [Campbell & Bozorgnia, 2014](#); [Abrahamson et al., 2014](#); [Boore et al., 2014](#); [Chiou & Youngs, 2014](#)).

Efforts to produce rapid 3D Green’s functions or seismic waveforms using interpolation or machine learning approaches have shown promise and have been improving in complexity the past few years. These machine learning approaches typically focus on solving some version of the seismic wave equation and have used various architectures including neural operators ([Yang et al., 2021, 2023](#); [Lehmann et al., 2024](#)), generative adversarial networks ([Shi et al., 2024](#); [Wang et al., 2021](#); [Florez et al., 2022](#)) and physics-informed neural networks ([Moseley et al., 2020](#); [Rasht-Behesht et al., 2022](#); [Smith et al., 2020](#)). However, no current method exists that is capable of performing regional scale physics-based ground motion prediction that incorporates detailed structural heterogeneities and topographic effects. Another important consideration is the time to solution of each method, and it remains unclear which approaches are best suited for producing rapid, high-resolution seismic wavefields for a realistic regional model domain. Instead of solving the wave equation, other approaches have used random forests and neural networks to create ground motion maps or ground motion models using simulated data ([Monterrubio-Velasco et al., 2024](#); [Withers et al., 2020](#)).

Reduced-order models (ROMs) offer an alternative approach by simplifying computations and reducing the amount of expensive numerical simulations described by partial differential equations, referred to as full-order models (FOMs). ROMs have been extensively applied in other fields of science and engineering (e.g., [Benner et al., 2015](#); [Hesthaven et al., 2022](#); [Willcox & Peraire, 2002](#)), as well as in seismology ([Pereyra & Kaelin, 2008](#); [Nagata et al., 2023](#); [Rekoske et al., 2023](#); [Hawkins et al., 2023](#); [Kusanovic et al., 2023](#)).

In this work, we develop an approach for producing rapid, high-resolution wavefields for a 3D seismic velocity model using an interpolated proper orthogonal decomposition reduced-order modeling approach. This approach substantially extends the method described in [Rekoske et al. \(2023\)](#) by including the handling of moving epicentral source locations, and generating complete 60-second velocity waveforms for a set of elementary moment tensors. It provides a flexible approach to rapidly generate approximate numerical Green’s functions, which in turn can be used to simulate seismograms for complex rupture models.

We apply this approach to produce Green’s functions for earthquake sources near the Whittier Fault Zone, where damaging earthquakes, including the 1987 Whittier Narrows blind thrust earthquake, have occurred. Seismic hazard assessments that use a set of fault locations may not accurately account for the hazard from these types of blind faults (e.g., [Hauksson & Jones, 1988](#); [Shaw & Shearer, 1999](#)). The seismic wavefields from these earthquakes affect a major metropolitan area, including part of the Los Angeles Basin, where local amplification effects are significant ([Komatitsch et al., 2004](#); [Field et al., 1997](#); [Moschetti et al., 2024](#)).

The organization of this paper is as follows: [Sec. 2](#) describes the procedures for obtaining the FOM and ROM seismograms, and the methods to quantitatively evaluate the accuracy of the ROM using leave-one-out

cross validation. Sec. 3 provides the seismogram results for three types of seismic sources: (1) an elementary moment tensor from the [Kikuchi & Kanamori \(1991\)](#) basis, (2) a general moment tensor, and (3) a kinematic rupture model with a heterogeneous slip distribution. Lastly, Sec. 4 discusses potential applications of this work for rapid wavefield predictions, compares our results to other relevant work, and outlines potential improvements for future research.

## 2 Methods

### 2.1 Full-order model (FOM): Seismic full waveform modeling using high-performance computing

To generate the synthetic seismogram data for this study, we perform full waveform modeling for a set of source and receiver locations in southern California. We here consider potential earthquakes occurring in a  $40 \times 14 \times 16$  km (length  $\times$  width  $\times$  depth) box which contains a portion of the Whittier Fault Zone (Fig. 1). We will consider hypocentral depths ranging from 4 to 20 km. In total we consider  $n_s = 500$  sources. The coordinates of the sources are described in Sec. 2.2. The receivers are located 1 meter below the Earth’s surface on a uniform grid with 500 m spacing, covering a 50 km by 40 km area, resulting in a total of  $n_r = 8,181$  receivers. The receivers are located throughout the densely populated greater Los Angeles area, and cover a variety of landscapes including the Los Angeles Basin, the San Gabriel Valley, the Santa Ana Mountains, and its foothills.

The seismic velocity model describing the P-wave speed ( $V_P$ ), S-wave speed ( $V_S$ ), and density ( $\rho$ ) for this study region was defined using the UCVM software ([Small et al., 2017](#)). We used a particular version of a community velocity model, CVM-S4.26.M01, that includes a geotechnical layer. This model was chosen based on results from [Taborda et al. \(2016\)](#), which indicated that this velocity model performed best for simulating previous earthquakes in southern California. We use a minimum S-wave speed of 500 m/s and 3D spatially variable quality factors of  $Q_S = 0.05V_S$  and  $Q_P = 0.1V_S$  (for  $V_S$  measured in m/s) to describe the attenuation of seismic waves ([Olsen et al., 2003](#)).

We model visco-elastic seismic wave propagation following the formulation of [Kristek & Moczo \(2003\)](#); [Moczo et al. \(2004\)](#) in which the constitutive behavior of the domain consists of an elastic body in parallel with  $L$  Maxwell (visco-elastic) bodies, and is governed by the following set of PDEs

$$\rho \frac{\partial \mathbf{v}}{\partial t} = \nabla \cdot \boldsymbol{\sigma}, \tag{1a}$$

$$\boldsymbol{\sigma} = \lambda \text{Tr}(\mathbf{E}(\mathbf{u}))\mathbf{I} + 2\mu\mathbf{E}(\mathbf{u}) - \sum_{l=1}^L (\lambda Y_l^\lambda \text{Tr}(\boldsymbol{\xi}^l)\mathbf{I} + 2\mu Y_l^\mu \boldsymbol{\xi}^l) + \mathbf{S}, \tag{1b}$$

$$\frac{\partial \boldsymbol{\xi}^l}{\partial t} = \omega_l \mathbf{E}(\mathbf{u}) - \omega_l \boldsymbol{\xi}^l, \tag{1c}$$



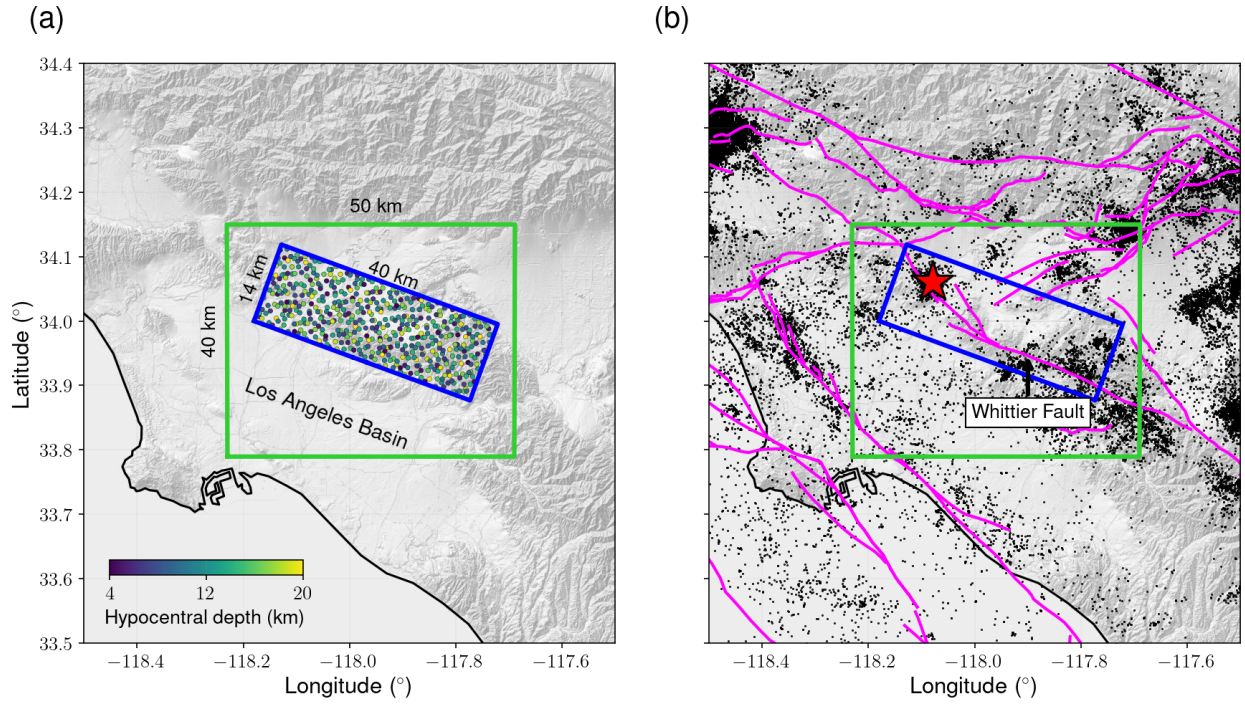


Figure 1: Map of the study area in Southern California used for computing rapid seismic wavefields. The source and receiver areas are indicated by blue and green rectangles, respectively. In (a), the earthquake source locations used for the simulations are indicated by the colored circles, where the color indicates hypocentral depths ranging from 4 to 20 km. We determine the latitude, longitude, and depths of the earthquakes using a pseudorandom Halton sequence. In (b), the black dots indicate locations of real earthquakes from the [Hauksson et al. \(2012\)](#) catalog, and the magenta lines indicate fault traces from the SCEC Community Fault Model ([Marshall et al., 2023](#)). The red star marks the epicenter of the 1987  $M_W$  5.9 Whittier Narrows earthquake, which we use as a demonstrator for our finite fault rupture modeling approach.

in which  $\mathbf{v}$  is the velocity,  $\boldsymbol{\sigma}$  is the stress,  $\boldsymbol{\xi}^l$  are the visco-elastic memory variables for each  $l$  mechanism,  $\mathbf{E}(\mathbf{u}) = \frac{1}{2}[\nabla\mathbf{u} + (\nabla\mathbf{u})^T]$  is the symmetric gradient of the displacement field  $\mathbf{u}$ ,  $\mathbf{I}$  is the identity and  $\text{Tr}(\cdot)$  denotes the trace operator. The density  $\rho$  and Lamé parameters  $\lambda$ ,  $\mu$  are spatially variable and determined using the values of  $\rho$ ,  $V_S$ ,  $V_P$  obtained from CVM-S4.26.M01. The variables  $\omega_l$  and  $Y_l^\lambda$ ,  $Y_l^\mu$  define the relaxation frequency and the anelastic analogs of Lamé parameters for each mechanism  $l$ . Following Käser et al. (2007) we define the spatially variable anelastic coefficients  $Y_l^\lambda$  and  $Y_l^\mu$  using

$$Y_\ell^\lambda = \left(1 + \frac{2\mu}{\lambda}\right) Y_\ell^P - \frac{2\mu}{\lambda} Y_\ell^S, \quad Y_\ell^\mu = Y_\ell^S, \quad (2)$$

and

$$Q_\alpha^{-1} = \sum_{\ell=1}^L \frac{\omega_\ell \omega_k + \omega_\ell^2 Q_\alpha^{-1}}{\omega_\ell^2 + \omega_k^2} Y_\ell^\alpha, \quad \alpha = P, S, \quad (3)$$

together with the assumptions of  $Q_S = 0.05V_S$  and  $Q_P = 0.1V_S$  which are defined for the central frequency  $\omega_k$ . The frequency-independent  $Q$  relationships derived in Olsen et al. (2003) describe long-period waves (0 - 0.5 Hz) in the Los Angeles Basin, thus, we assumed a central frequency  $\omega_k$  of 0.2 Hz.

In Eq. (1b) the moment tensor seismic source is denoted by  $\mathbf{S}$ . We assume point sources, thus, it is convenient to decompose  $\mathbf{S}$  into a time varying component  $M(t)$ , a constant tensor  $\bar{\mathbf{M}}$  and a spatial component resulting in

$$\mathbf{S} = M(t)\bar{\mathbf{M}}\delta(\mathbf{x} - \mathbf{p}), \quad (4)$$

where  $\mathbf{p}$  denotes the physical location of the source. To facilitate representing general moment tensor sources, we exploit the seismic moment tensor decomposition of Kikuchi & Kanamori (1991) given by

$$\bar{\mathbf{M}} = \sum_{i=1}^6 c_i \widehat{\mathbf{M}}_i,$$

in which  $\widehat{\mathbf{M}}_i$  are referred to as the elementary moment tensors and  $c_i$  are the weights. The definition of the elementary moment tensors is provided in Appendix A and the beachball plots of the six elementary tensors are shown in Fig. 2. The moment tensor decomposition can be inverted – that is, given an arbitrary (symmetric) tensor  $\bar{\mathbf{M}}$  such as

$$\bar{\mathbf{M}} = \begin{bmatrix} M_{11} & M_{12} & M_{13} \\ M_{12} & M_{22} & M_{23} \\ M_{13} & M_{23} & M_{33} \end{bmatrix}, \quad (5)$$

a unique set of weights  $c_i$  can be obtained by solving the following linear system

$$\begin{bmatrix} 0 & 1 & 0 & 0 & -1 & 1 \\ 1 & 0 & 0 & 0 & 0 & 0 \\ 0 & 0 & 0 & 1 & 0 & 0 \\ 0 & -1 & 0 & 0 & 0 & 1 \\ 0 & 0 & 1 & 0 & 0 & 0 \\ 0 & 0 & 0 & 0 & 1 & 1 \end{bmatrix} \begin{bmatrix} c_1 \\ c_2 \\ c_3 \\ c_4 \\ c_5 \\ c_6 \end{bmatrix} = \begin{bmatrix} M_{11} \\ M_{12} \\ M_{13} \\ M_{22} \\ M_{23} \\ M_{33} \end{bmatrix}. \quad (6)$$

Any general moment tensor can be reconstructed using a combination of the six elementary tensors. One advantage of this decomposition is that some sources may not require all six components. For example, only two components are required for pure strike-slip earthquakes, and only five components are required for pure double-couple sources (Kikuchi & Kanamori, 1991). We note that here, our method slightly differs from CyberShake simulations (e.g., Graves et al., 2011; Milner et al., 2021; Jordan & Callaghan, 2018) where SGTs are computed for only dip-slip and strike-slip components for assumed fault orientations. We use the moment rate as a function of time  $t$  given by  $\dot{M}(t) = \frac{M_0 t}{T^2}$  with  $M_0 = 1.0 \times 10^{15}$  N m and  $T = 0.34$  s. In the frequency domain, this source has a Brune-like spectrum corresponding to a stress drop of approximately 5.0 MPa (Brune, 1970).

Lastly we note that Eqs. (1) are linear in the velocity  $\mathbf{v}$ , stress  $\boldsymbol{\sigma}$  and  $\boldsymbol{\xi}^l$ , hence we can apply the principle of linear superposition. That is, given a set of  $k = 1, \dots, N$  source terms  $\mathbf{S}_k$  of the form shown in Eq. (4), the resulting solutions  $\mathbf{v}_1, \dots, \mathbf{v}_N$ ,  $\boldsymbol{\sigma}_1, \dots, \boldsymbol{\sigma}_N$  and  $\boldsymbol{\xi}_1^l, \dots, \boldsymbol{\xi}_N^l$  can be linearly combined such that  $\mathbf{v} = \sum_{k=1}^N \mathbf{v}_k$ ,  $\boldsymbol{\sigma} = \sum_{k=1}^N \boldsymbol{\sigma}_k$ ,  $\boldsymbol{\xi}^l = \sum_{k=1}^N \boldsymbol{\xi}_k^l$  is the solution to Eqs. (1) with  $\mathbf{S} = \sum_{k=1}^N \mathbf{S}_k$ .

We solve Eqs. (1) using SeisSol ([www.seissol.org](http://www.seissol.org)), an open-source software for numerical simulation of seismic wave propagation and earthquake dynamics. SeisSol uses the Arbitrary high-order accurate DERivative Discontinuous Galerkin method (ADER-DG) (Käser & Dumbser, 2006; Dumbser & Käser, 2006; Käser et al., 2007) and end-to-end optimization for high-performance computing infrastructure (Heinecke et al., 2014; Uphoff & Bader, 2016; Uphoff et al., 2017; Rettenberger et al., 2016). SeisSol employs fully unstructured tetrahedral meshes which allow for geometrically complex 3D geological structures and topography to be accurately resolved. We use velocity-aware meshing (Breuer & Heinecke, 2022) to create a mesh consisting of about 3.5 million tetrahedral elements that accurately resolves frequencies up to 0.5 Hz. This estimate is based on requiring six elements per shortest wavelength according to the numerical accuracy analysis of SeisSol’s modal ADER-DG approach performed by Käser et al. (2008). Within the visco-elastic framework used we consider three damping mechanisms ( $L = 3$ ) with relaxation frequencies of  $\omega_1 = 0.02$  Hz,  $\omega_2 = 0.2$  Hz, and  $\omega_3 = 2.0$  Hz. The value of  $\omega_L$  (maximum frequency) is typically the upper bound for which  $Q$  is assumed to be frequency-independent. We used a value of  $\omega_L$  which is slightly higher than the largest frequency resolvable with our mesh to ensure  $Q$  is frequency-independent in our band of interest. The choice of  $L = 3$  with logarithmically spaced relaxation frequencies was taken as this configuration is known to be

sufficient to achieve less than 5% error in the frequency band of interest (Emmerich & Korn, 1987).

The computational cost per simulation is approximately 192 central processing unit hours (CPUh) per point source location using a degree four polynomial in space and time. All numerical simulations were performed on SuperMUC-NG using single precision. For each seismic source, we simulate 60 seconds of wave propagation. For all six elementary tensors and for all  $n_s = 500$  source locations, the total cost of generating the synthetic data was approximately 576,000 CPUh. The number of receivers is much larger than the number of sources, thus, we run the simulations in a forward sense and not a reciprocal sense. From each simulation, we save the 60-second velocity waveforms, sampled at 10 Hz, for each of the 8,181 receivers. We postprocess the timeseries data using a linear, fourth-order, Butterworth low-pass filter at 0.5 Hz. We apply the filter both forwards and backwards to ensure zero phase shift of the waveform data.

SeisSol can also compute synthetic seismograms for finite earthquake sources that are described by a set of point sources, such as kinematic rupture models. Examples of these finite sources can be found at the SRCMOD database (Mai & Thingbaijam, 2014). When simulating finite sources the moment rate function at each point source may be variable. When considering finite sources, we do not apply any upsampling in space, meaning that we use the same number of moment tensors in our forward simulations as are provided in the original rupture models. The exact computation time per forward simulation of a finite source may slightly vary depending on the source description, though we found that when using a model composed of 100 point sources, the computation time was approximately the same at 198 CPUh.

## 2.2 Reduced-order model (ROM)

The ROM that we present in this study is a computationally inexpensive, data-driven technique to produce seismic wavefields for earthquakes in our study region. We build the ROM from the synthetic data (simulated surface velocity waveforms) generated for a set of  $n_s = 500$  sources located within the volume  $\mathcal{P}$  for the six elementary moment tensors. We denote each source location by the vector  $\mathbf{p}_i$  given by

$$\mathbf{p}_i = \begin{bmatrix} \Delta\ell_i \\ \Delta w_i \\ \Delta z_i \end{bmatrix}, \quad i = 1, \dots, n_s, \quad (7)$$

where  $\Delta\ell_i, \Delta w_i$ , and  $\Delta z_i$  denote the three distances to the sides of the box  $\mathcal{P}$  (see Fig. 2). We prescribe the locations of the earthquake sources in three dimensions using a pseudorandom Halton sequence, which efficiently fills the entire volume  $\mathcal{P}$ . The locations of the sources generated by the Halton sequence are shown in Fig. 1.

After performing all the wave propagation simulations for these sources, as described by the FOM procedure in Sec. 2.1, we gather all lowpass-filtered receiver timeseries data into matrices  $\mathbf{D}_{i,j}$  where  $i = 1, \dots, 6$  indicates the elementary tensor index and  $j = 1, 2, 3$  indicates the component of the wavefield ( $j = 1$  is the

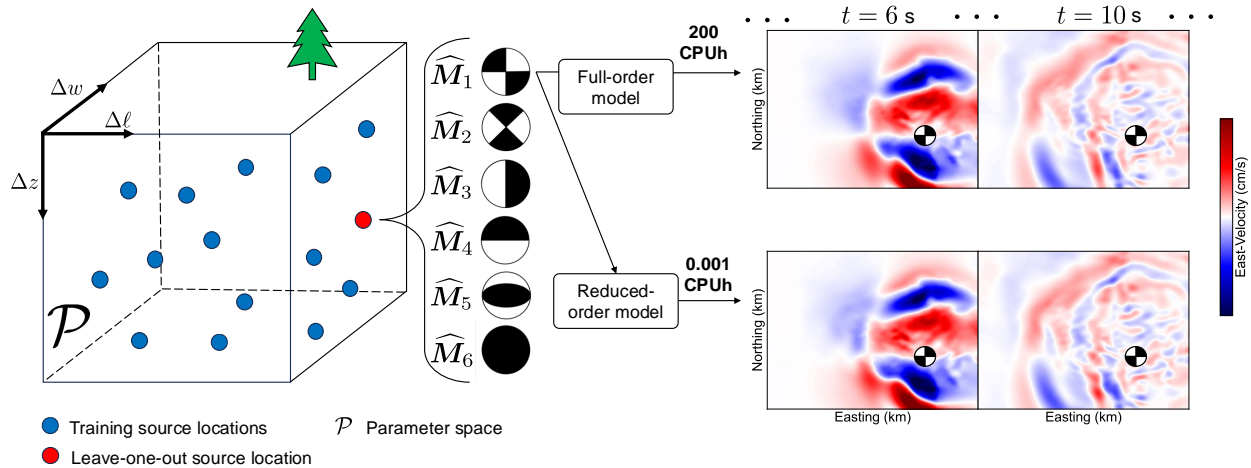


Figure 2: Conceptual illustration of the ROM workflow for producing and verifying rapid simulations of seismic wave propagation. Within the 3D volume defined by  $\mathcal{P}$ , we simulate forward wave propagation defined by the full-order model (FOM) for a set of  $n_s$  source locations located in the volume, indicated by the colored circles. The source locations are identified by the parameters  $\Delta \ell$ ,  $\Delta w$ , and  $\Delta z$  which indicate the distances from the sides of the box  $\mathcal{P}$  and are determined using a pseudorandom Halton sequence. For each source location, we run six expensive ( $\approx 200$  CPUh each) 60-second simulations for each elementary moment tensor (Kikuchi & Kanamori, 1991) indicated by the black-and-white beachballs, and store the three-component velocity wavefield at the surface. The ROM is a computationally inexpensive ( $\approx 0.001$  CPUh) approximation of the FOM. We quantify the accuracy of the ROM with leave-one-out cross validation.

$u$ -component,  $j = 2$  is the  $v$ -component, and  $j = 3$  is the  $w$ -component). We denote  $\mathbf{D}_{ij}$  as

$$\mathbf{D}_{ij} = \left[ \mathbf{q}_{ij}(\mathbf{p}_1), \mathbf{q}_{ij}(\mathbf{p}_2), \dots, \mathbf{q}_{ij}(\mathbf{p}_{n_s}) \right], \quad (8)$$

where  $\mathbf{q}_{ij}$  is a vector containing the surface velocity timeseries data, produced by the FOM, for all  $n_r = 8,181$  receivers and all  $n_t = 600$  time steps. Thus, each  $\mathbf{D}_{ij}$  contains  $n_r \times n_t = 8,181 \times 600 = 4,908,600$  rows and  $n_s = 500$  columns. We then compute the singular value decomposition (SVD) of each  $\mathbf{D}_{ij}$ ,

$$\mathbf{D}_{ij} = \mathbf{U}_{ij} \mathbf{\Sigma}_{ij} \mathbf{V}_{ij}^T, \quad (9)$$

where  $\mathbf{U}_{ij}$  contains the left singular vectors (also known as modes),  $\mathbf{\Sigma}_{ij}$  contains the singular values, and  $\mathbf{V}_{ij}$  contains the right singular vectors. We emphasize that our approach considers the SVD for each elementary tensor and velocity component separately as the total size of the simulated data is approximately  $\approx 177$  GB.<sup>1</sup> A further computational saving is made by not computing the SVD directly, but rather computing the eigen decomposition of  $\mathbf{C}_{ij} = \mathbf{D}_{ij}^T \mathbf{D}_{ij}$ . The singular values  $\mathbf{\Sigma}_{ij}$  are given by the square root of the eigenvalues of  $\mathbf{C}_{ij}$ , and the right singular vectors,  $\mathbf{V}_{ij}$ , are equal to the eigenvectors of  $\mathbf{C}_{ij}$ . We can obtain the left singular vectors by solving Eq. (9) for  $\mathbf{U}_{ij}$ .

The act of computing the SVD of the data matrices  $\mathbf{D}_{ij}$  defines a set of (discrete) spatial basis functions (the left singular vectors), along with weights of coefficients (singular values and right singular vectors) which can be used to reconstruct any column in  $\mathbf{D}_{ij}$ . This interpretation of the SVD is connected with the term Proper Orthogonal Decomposition (POD) coined in the seminal model order reduction literature (e.g, Berkooz et al., 1993; Bui-Thanh et al., 2003; Druault et al., 2005).

After computing the singular values and right singular vectors, we define the POD coefficients as the matrix  $\mathbf{A}_{ij}$  given by

$$\mathbf{A}_{ij} = \mathbf{V}_{ij} \mathbf{\Sigma}_{ij}. \quad (10)$$

We follow Rekoske et al. (2023) to interpolate the POD coefficients using radial basis functions (RBFs) (e.g, Lazzaro & Montefusco, 2002; Audouze et al., 2009; Xiao et al., 2015). That is, the interpolator function for the  $k$ -th mode associated with  $\mathbf{A}_{ij}$  is

$$\tilde{A}_{ijk}(\mathbf{p}) = \sum_{l=1}^{n_s} w_{ijkl} \varphi(\|\mathbf{p} - \mathbf{p}_l\|_2) + \sum_{m=1}^{|V|} b_{ijkm} \psi_m(\mathbf{p}), \quad (11)$$

where the function  $\varphi(\cdot)$  is an RBF,  $w_{ijkl}$  is an entry of the kernel weight matrix  $\mathbf{W}_{ij}$ ,  $b_{ijkm}$  is an entry of the polynomial coefficient matrix  $\mathbf{B}_{ij}$ , and  $\psi_m(\cdot)$  are monomial terms up to a specified degree  $d$  contained

<sup>1</sup>All elements of  $\mathbf{D}_{ij}$  are represented via the `float` datatype (4 bytes).

in the set  $V$  given by

$$V = \{ \Delta \ell^r \Delta w^s \Delta z^t \mid r + s + t \leq d \text{ with } r \geq 0, s \geq 0, t \geq 0 \}. \quad (12)$$

We determine the coefficients contained in  $\mathbf{W}_{ij}$  and  $\mathbf{B}_{ij}$  by solving the system of linear equations

$$\Phi \mathbf{W}_{ij} + \Psi \mathbf{B}_{ij} = \mathbf{A}_{ij}, \quad (13a)$$

$$\Psi^T \mathbf{B}_{ij} = \mathbf{0}, \quad (13b)$$

where

$$\Phi = \begin{bmatrix} \varphi(\|\mathbf{p}_1 - \mathbf{p}_1\|_2) & \varphi(\|\mathbf{p}_2 - \mathbf{p}_1\|_2) & \cdots & \varphi(\|\mathbf{p}_{n_s} - \mathbf{p}_1\|_2) \\ \varphi(\|\mathbf{p}_1 - \mathbf{p}_2\|_2) & \varphi(\|\mathbf{p}_2 - \mathbf{p}_2\|_2) & \cdots & \varphi(\|\mathbf{p}_{n_s} - \mathbf{p}_2\|_2) \\ \vdots & \vdots & \ddots & \vdots \\ \varphi(\|\mathbf{p}_1 - \mathbf{p}_{n_s}\|_2) & \varphi(\|\mathbf{p}_2 - \mathbf{p}_{n_s}\|_2) & \cdots & \varphi(\|\mathbf{p}_{n_s} - \mathbf{p}_{n_s}\|_2) \end{bmatrix}, \quad (14)$$

and  $\Psi$  is the matrix of polynomials up to degree  $d$ . For the RBFs  $\varphi(\cdot)$ , we test four types of kernels: linear ( $\varphi(r) = r$ ), thin plate spline ( $\varphi(r) = r^2 \ln(r)$ ), cubic ( $\varphi(r) = r^3$ ) and quintic ( $\varphi(r) = -r^5$ ). For each kernel, we solve the linear system using the minimum polynomial degree, i.e.,  $d = 0$  for linear,  $d = 1$  for the thin plate spline and cubic kernels, and  $d = 2$  for the quintic kernel.

To generate seismic waveforms using the ROM for a new source location given by  $\mathbf{p}^*$ , for an elementary moment tensor, we can perform a reconstruction using the POD basis (i.e. the left singular vectors) via

$$\tilde{\mathbf{q}}_{ij}(\mathbf{p}^*) = \sum_{k=1}^{n_s} \tilde{A}_{ijk}(\mathbf{p}^*) \mathbf{u}_{ijk}, \quad (15)$$

where  $\mathbf{u}_{ijk}$  indicates the left singular vector from the matrix  $\mathbf{U}_{ij}$  for the  $k$ -th mode.  $\tilde{\mathbf{q}}_{ij}$  then contains the predicted data for the  $i$ -th elementary tensor and the  $j$ -th wavefield component, and the tilde indicates that this is an approximation.

To simulate seismic waveforms via the ROM for a source described by a general moment tensor  $\bar{\mathbf{M}}$ , we first obtain the weights  $c_i$  by solving Eq. (6) where  $c_i$  is the weight corresponding to the  $i$ -th elementary tensor, and then compute

$$\tilde{\mathbf{q}}_j(\mathbf{p}^*) = \sum_{i=1}^6 c_i \tilde{\mathbf{q}}_{ij}(\mathbf{p}^*), \quad (16)$$

where the  $\tilde{\mathbf{q}}_{ij}$  are obtained using Eq. (15). That is, we weight the ROM solution obtained from each elementary tensor  $i$  by  $c_i$ . If any of the  $c_i$  are equal to zero, then all six components might not be needed in Eq. (16).

### 2.3 Training and validation procedure: leave-one-out cross validation

To quantify the accuracy of the rapid seismic wavefields obtained from the ROM, we use a leave-one-out cross-validation (LOOCV) procedure (Rippa, 1999). One advantage of using RBFs as an interpolator function is that it is relatively cheap to perform this type of analysis using the Rippa (1999) algorithm, compared to machine learning techniques where re-training models can be very costly. The Rippa (1999) LOOCV procedure is outlined below:

1. Write the system in Eq. (13) as

$$\begin{pmatrix} \Phi & \Psi \\ \Psi^T & \mathbf{0} \end{pmatrix} \begin{pmatrix} \mathbf{W}_{ij} \\ \mathbf{B}_{ij} \end{pmatrix} = \begin{pmatrix} \mathbf{A}_{ij} \\ \mathbf{0} \end{pmatrix} \rightarrow \mathbf{\Gamma} \mathbf{X}_{ij} = \mathbf{F}_{ij}, \quad (17)$$

where  $\mathbf{X}_{ij}$  and  $\mathbf{F}_{ij}$  represent a matrix of solutions and right-hand sides, respectively. We then note that  $\mathbf{\Gamma}$  is identical for every elementary moment tensor  $i$  and wavefield component  $j$ . Given this, it is efficient to factor  $\mathbf{\Gamma}$  once using a stable decomposition such as the Cholesky decomposition or SVD, and then apply the action of the inverse decomposition to obtain each  $\mathbf{X}_{ij}$ .

2. Re-use the factored form of  $\mathbf{\Gamma}$  to compute  $\mathbf{v}$ , defined as the first  $n_s$  components of the diagonal of  $\mathbf{\Gamma}^{-1}$ .
3. Compute the leave-one-out predictions for the POD coefficients via

$$\tilde{A}_{ijk}(\mathbf{p}_l) = A_{ijkl} - w_{ijkl} \odot \frac{1}{v_l}, \quad (18)$$

where  $A_{ijkl}$  indicates the POD coefficient from  $\mathbf{A}_{ij}$  that corresponds to the  $k$ -th mode and the  $l$ -th source location and  $\odot$  indicates an element-wise product.

4. Use Eq. (15) to compute the predicted data  $\tilde{\mathbf{q}}_{ij}(\mathbf{p}_l)$  using the predicted POD coefficients  $\tilde{A}_{ijk}$  and left singular vectors  $\mathbf{U}_{ij}$ .

In addition to the LOOCV error, we also compute the following accuracy metrics for the mean absolute velocity error (MAVE), mean peak ground velocity error (MPGVE), and the mean spectral error (MSE):

$$\text{MAVE}_{ij}(\mathbf{p}) = \frac{1}{n_r n_t} \|\mathbf{q}_{ij}(\mathbf{p}) - \tilde{\mathbf{q}}_{ij}(\mathbf{p})\|_1, \quad (19)$$

$$\text{MPGVE}_{ij}(\mathbf{p}) = \frac{1}{n_r} \left\| \max_t |\mathbf{q}_{ij}(\mathbf{p})| - \max_t |\tilde{\mathbf{q}}_{ij}(\mathbf{p})| \right\|_1, \quad (20)$$

$$\text{MSE}_{ij}(\mathbf{p}, f) = \frac{1}{n_r} \left\| \hat{\mathbf{q}}_{ij}(\mathbf{p}, f) - \hat{\tilde{\mathbf{q}}}_{ij}(\mathbf{p}, f) \right\|_1. \quad (21)$$

Here,  $\hat{\mathbf{q}}_{ij}(\mathbf{p}, f)$  indicates the Fourier transform of the FOM velocity timeseries as a function of frequency  $f$ . We compute the FFTs using `numpy.fft.rfft`, take the absolute value, then normalize by multiplying by the sampling interval of 0.1 s.



## 2.4 Approximate Green's function calculations

The seismograms that can be computed directly using our ROM correspond to a particular moment rate function. If we instead had used a delta function for the source time function, then the seismograms would be mathematically equivalent to the Green's function; however, it is often more numerically stable to use a smooth source time function with a fixed width (e.g., Igel, 2017; van Driel et al., 2015). Since it is often required to simulate seismograms for rupture models with different moment rates, we compute the elastodynamic Green's functions by deconvolving the prescribed source time function from the seismograms. Following Aki & Richards (2002), our simulated velocity seismograms can be expressed as a convolution of the source's moment rate function and a Green's function,

$$\mathbf{q}_{ij}(\mathbf{p}) = \dot{M} * \mathbf{G}_{ij}(\mathbf{p}). \quad (22)$$

Here,  $\mathbf{G}_{ij}(\mathbf{p})$  contains the time-dependent Green's functions for all receiver locations for the source located at  $\mathbf{p}$ . Using the convolution theorem, we obtain

$$\mathbf{G}_{ij}(\mathbf{p}) = \mathcal{F}^{-1} \left\{ \frac{\mathcal{F} \{ \mathbf{q}_{ij}(\mathbf{p}) \}}{\mathcal{F} \{ \dot{M} \}} \right\} \quad (23)$$

where  $\mathcal{F}$  indicates the Fourier transform. Replacing the FOM seismograms with the ROM-predicted seismograms, we obtain the approximate Green's functions,

$$\tilde{\mathbf{G}}_{ij}(\mathbf{p}) = \mathcal{F}^{-1} \left\{ \frac{\mathcal{F} \{ \tilde{\mathbf{q}}_{ij}(\mathbf{p}) \}}{\mathcal{F} \{ \dot{M} \}} \right\}. \quad (24)$$

Thus, we can use the computed equivalent Green's functions to rapidly approximate the simulated data from finite fault rupture models using the discrete representation theorem (Aki & Richards, 2002). For example, if we have a rupture model consisting of  $n_f$  subfaults, where each subfault may have a different source time function ( $\dot{M}^k$ ), the general formula for the obtaining the predicted velocity timeseries for component  $j$  is given by

$$\tilde{\mathbf{q}}_j = \sum_{k=1}^{n_f} \sum_{i=1}^6 c_i^k \dot{M}^k * \tilde{\mathbf{G}}_{ij}(\mathbf{p}_k), \quad (25)$$

where  $c_i^k$  indicates the weight for the  $i$ -th elementary moment tensor for the  $k$ -th subfault.

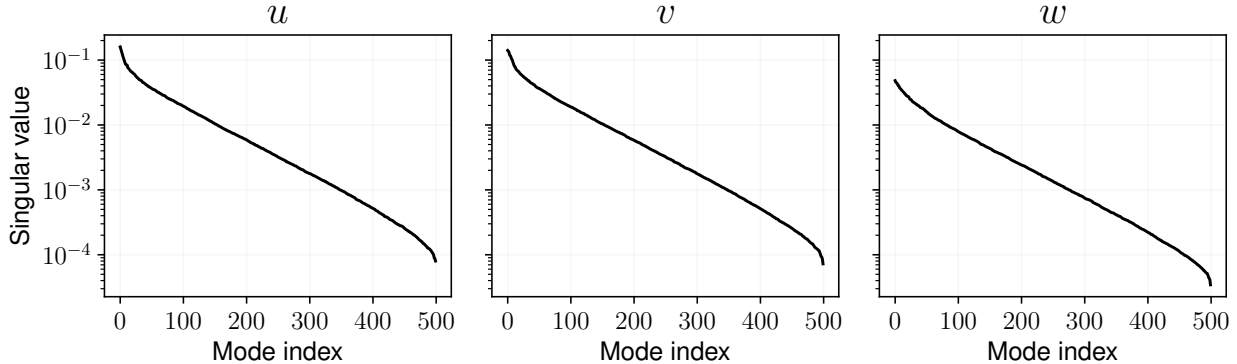


Figure 3: Singular value spectra obtained by taking the SVD of the data matrices which contain the FOM seismograms corresponding to the east ( $u$ ), north ( $v$ ), and vertical ( $w$ ) components of the seismic wavefield, respectively. The singular values are shown for the simulated seismograms associated with the  $\widehat{\mathbf{M}}_1$  elementary moment tensor source (see Appendix A for the definitions of the elementary moment tensors).

### 3 Results

#### 3.1 Singular value spectra of the simulated seismograms

Taking the SVD of the data matrices of simulated seismograms allows us to obtain the singular values which provide important understanding of the properties and structure of each data matrix. Specifically, the singular values indicate how important the information is that is contained in each of the modes. The singular values for the  $\widehat{\mathbf{M}}_1$  elementary moment tensor (a pure strike-slip fault) associated with each velocity component are shown in Fig. 3. The singular values for each velocity component decrease rapidly over the first 20 indices, and then decay with an apparent log-linear slope. We infer that the data matrices have (approximately) full rank, since the singular values over the entire spectrum do not decay exponentially fast. As expected, the singular values for the  $w$ -component (vertical) are generally smaller than the singular values for the horizontal components due to the smaller amplitudes of the seismic waves on the vertical component.

When plotted in depth slices, the POD coefficients appear as smooth maps of varying positive and negative amplitudes that can be accurately interpolated (Fig. 4). Following the definition of the POD, we see that the amplitudes of the POD coefficients decrease as the index of the mode increases due to the ordering of the singular values. Also, the coefficients decrease in amplitude for deeper earthquakes, which is also expected due to the decrease in ground motion amplitudes for deeper earthquakes.

#### 3.2 FOM and ROM accuracy analysis for an elementary moment tensor source

Using the interpolator functions to predict POD coefficients, we can now inspect how accurately the rapid seismic wavefields produced by the ROM match our high-resolution FOM simulations. We first inspect the wavefields that are produced by a point source  $\widehat{\mathbf{M}}_1$  elementary moment tensor. We select the results for

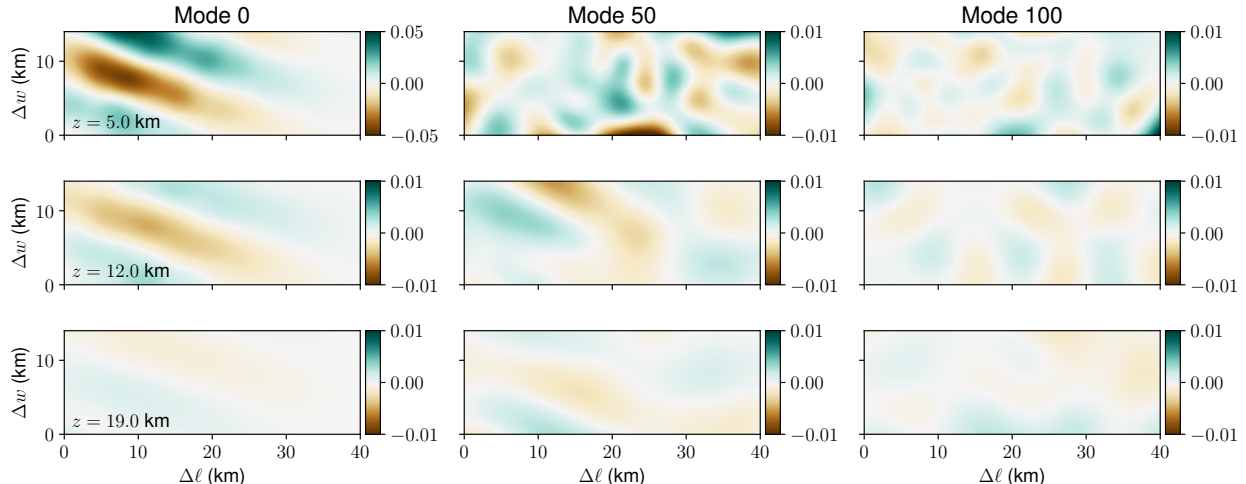


Figure 4: Views of the POD coefficients predicted by the RBFs for three different depth slices at  $z = (5, 12,$  and  $19)$  km. The results are shown for the quintic RBF kernel for the first elementary moment tensor and the east-component of the wavefield. The amplitudes of the POD coefficients are smaller for deeper earthquakes and for the higher-order modes (note the change in color scale in the top left panel which shows the Mode 0 coefficients for the shallow depth).

the first source location from the Halton sequence as an example. This source is located at  $(\Delta\ell = 3.5$  km,  $\Delta w = 9.9$  km,  $\Delta z = 12.5$  km). The ROM wavefield errors are evaluated using the [Rippa \(1999\)](#) algorithm for leave-one-out cross-validation as described in [Sec. 2.3](#).

[Fig. 5](#) shows map-view comparisons of the ROM and FOM surface wavefields at different timesteps of the simulation, as well as ground motion intensity maps. In these results, we scaled the waveform amplitudes to correspond to an  $M_W = 5$  earthquake (i.e., we multiplied them by a factor of 50). The FOM and ROM show good agreement in the velocity wavefields across all timesteps. The timing and amplitudes of the seismic wave arrivals in the FOM are well reproduced by the ROM. For this particular source location, a pronounced velocity pulse travels southward from the epicenter, which results in the strongest ground shaking in that direction. This amplification is likely influenced by the Los Angeles Basin and local site effects that affect ground motions in the southwest. Additionally, we observe significant scattering of the wavefield, particularly apparent at 14 s simulation time, which is expected due to the uneven topography and heterogeneity in the complex velocity model used.

Interestingly, the error (FOM - ROM) maps exhibit wave-like behavior, which is likely due to the absolute amplitudes of the waves being slightly under-predicted. Positive velocities (red) tend to correspond to green areas (FOM > ROM), and negative velocities (blue) tend to correspond to pink areas (FOM < ROM). Overall, the ROM generally under-predicts the strength of ground motion velocity as seen in the  $\max_t |u|$  map. However, this under-prediction reaches only about 5% at worst. Despite these minor inaccuracies, the FOM and ROM maintain good agreement throughout the different geological features and various landscapes

in our model domain.

The overall good fit of ROM ground motion levels to the FOM data is also evident in the Fourier amplitude spectra of the velocity seismograms (Fig. 7). We computed the spectra by taking the Fourier transform of the velocity data, taking the absolute value, and then multiplying by the sampling interval of 0.1 s. We did not apply any smoothing to the spectra. The spectral amplitudes at 0.2 Hz and 0.5 Hz show some slight under-prediction, as seen in the green areas in the right column of Fig. 5. In all ground motion maps, stronger shaking occurs in the western half of the simulation domain, which is also where ROM errors are larger. Errors tend to be close to zero in the east, while under-prediction in the west reaches 0.05 cm/s for  $\max_t |u|$  at worst, and 0.05 cm for the spectra at 0.2 and 0.5 Hz. At the higher frequency, the error is more spatially variable and the ROM may alternate between over- and under-prediction across short distances of less than 1 km.

By averaging across all of the  $n_s$  discrete source locations, we can compute the mean values for the MAVE, MPGVE, and MSE metrics (as defined in Sec. 2.3) for each  $j$  velocity component via

$$\overline{\text{MAVE}}_j = \frac{1}{n_s} \sum_{i=1}^{n_s} \text{MAVE}_j(\mathbf{p}_i), \quad (26)$$

$$\overline{\text{MPGVE}}_j = \frac{1}{n_s} \sum_{i=1}^{n_s} \text{MPGVE}_j(\mathbf{p}_i), \quad (27)$$

$$\overline{\text{MSE}(f)}_j = \frac{1}{n_s} \sum_{i=1}^{n_s} \text{MSE}_j(\mathbf{p}_i, f). \quad (28)$$

The results are summarized in Table 1 for the four RBF kernels that we tested (linear, cubic, quintic, and thin plate spline). We tabulate the mean errors when the ROM-predicted data are simply equal to the FOM data for the simulation using the nearest-neighboring source location (“nearest” column).

As shown, the cubic kernel gives the lowest  $\overline{\text{MAVE}}$  for all three components. When averaging over sources, receivers, and time steps, the  $\overline{\text{MAVE}}$  is about 0.007 cm/s for the two horizontal components and about 0.004 cm/s for the vertical component. The cubic kernel also gives the lowest  $\overline{\text{MSE}}$  when evaluated at 0.5 Hz. The quintic kernel performs the best for the  $\overline{\text{MPGVE}}$  metric and the  $\overline{\text{MSE}}$  metric for 0.2 Hz. We discuss these results further in Sec. 4, comparing our results against empirical GMMs and other ML approaches.

We examine the spatial trends in the source-averaged errors in Fig. 6. For all metrics, the errors tend to be largest closer to the center of the domain and smallest in the furthest corners. One exception is the southwest corner where the Los Angeles basin is likely amplifying ground motion. Interestingly, the error also correlates with some topographic features. This could be due to a correlation between topography and seismic wave speeds near the surface, or due to topographic amplification and shielding effects (e.g., Chaljub et al., 2010; Hartzell et al., 2014). For example, receivers in the Los Angeles Basin and San Gabriel Valley show higher errors than receivers located in the Puente Hills and other foothills of the Santa Ana and San

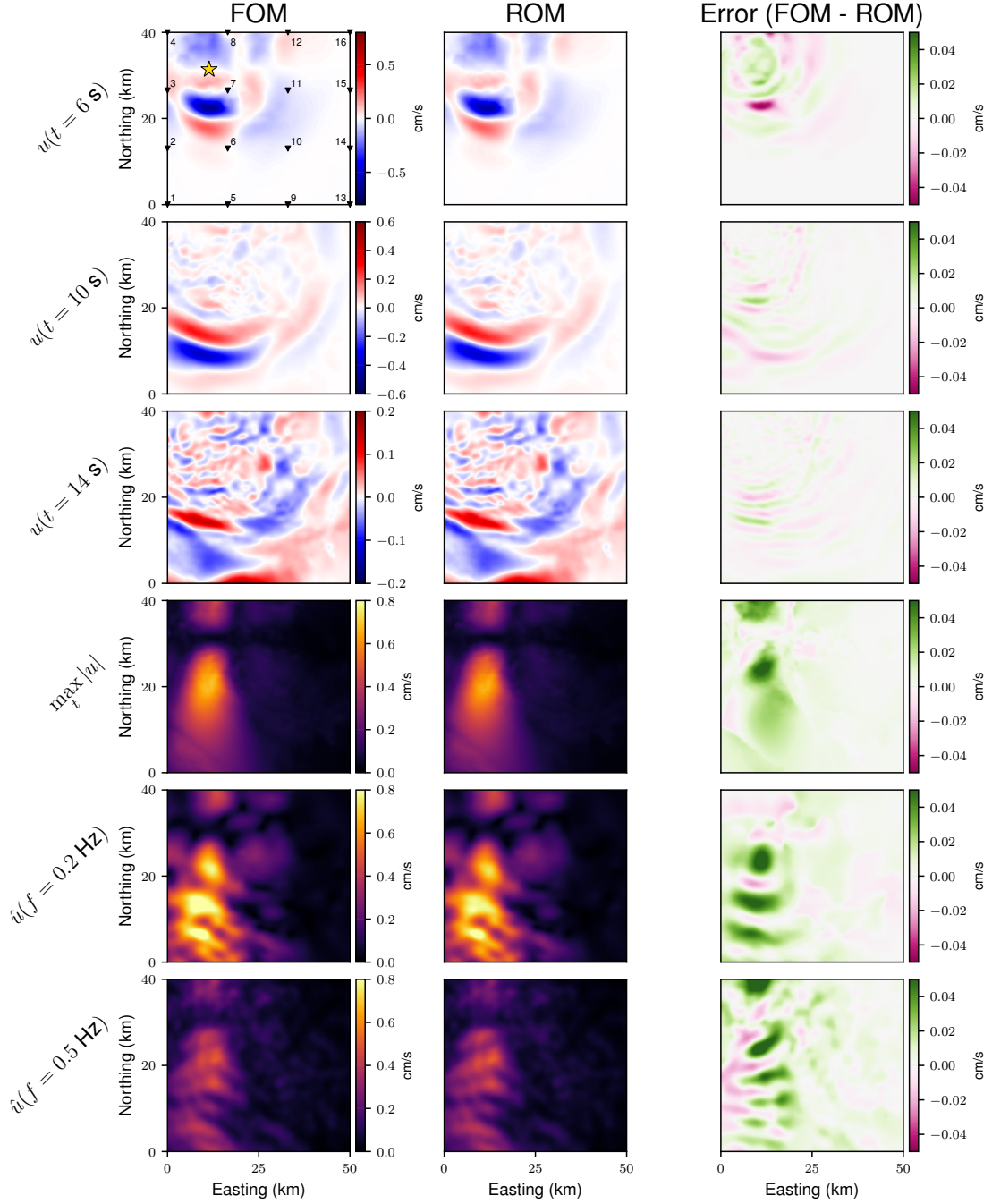


Figure 5: Surface wavefield snapshots and ground motion intensity maps, comparing the FOM results (left column), ROM results (middle column), and the difference between them (FOM - ROM, right column). The east-component ( $u$ ) of the velocity wavefields are shown in the first three rows. The fourth row shows the maximum absolute velocity over all time steps, and the fifth and sixth rows show the Fourier amplitudes at 0.2 and 0.5 Hz. The source is an  $M_W = 5.0$  earthquake with the same focal mechanism as the  $\widehat{M}_1$  elementary tensor. The source location is indicated by the gold star in the top left panel, and has a depth of 12.6 km. The locations of sixteen receivers used in subsequent plots are indicated by the black triangles in the top left panel. An animated movie of the FOM and ROM velocity wavefields showing all time steps is provided in the supplementary Movie S1.

	nearest	linear	cubic	quintic	thin plate spline
$\overline{\text{MAVE}}_1$	0.0135	0.0085	<b>0.0069</b>	0.0073	0.0072
$\overline{\text{MAVE}}_2$	0.0128	0.0081	<b>0.0067</b>	0.007	0.0069
$\overline{\text{MAVE}}_3$	0.0079	0.0051	<b>0.0043</b>	0.0046	0.0044
$\overline{\text{MPGVE}}_1$	0.0471	0.0516	0.0303	<b>0.0278</b>	0.0359
$\overline{\text{MPGVE}}_2$	0.0446	0.0477	0.0286	<b>0.0265</b>	0.0335
$\overline{\text{MPGVE}}_3$	0.0235	0.0203	0.0142	<b>0.0141</b>	0.0157
$\overline{\text{MSE}}(f = 0.2 \text{ Hz})_1$	0.0985	0.0687	0.0503	<b>0.0454</b>	0.056
$\overline{\text{MSE}}(f = 0.2 \text{ Hz})_2$	0.0964	0.0676	0.0496	<b>0.0444</b>	0.0554
$\overline{\text{MSE}}(f = 0.2 \text{ Hz})_3$	0.06	0.0402	0.0279	<b>0.0244</b>	0.0318
$\overline{\text{MSE}}(f = 0.5 \text{ Hz})_1$	0.0595	0.0837	<b>0.0534</b>	0.0552	0.0607
$\overline{\text{MSE}}(f = 0.5 \text{ Hz})_2$	0.0559	0.0775	<b>0.0500</b>	0.0522	0.0565
$\overline{\text{MSE}}(f = 0.5 \text{ Hz})_3$	0.0309	0.0355	<b>0.0237</b>	0.0239	0.0267

Table 1: Summary of the mean absolute velocity error (MAVE), mean peak ground velocity error (MPGVE), and mean spectral error (MSE) obtained from leave-one-out cross-validation for different interpolators. The errors are reported in cm/s for MAVE and MPGVE, and in cm for MSE. The velocity waveform amplitudes have been scaled to correspond to an  $M_W$  5.0 earthquake. The error measurements indicate the averages for all source locations, all receivers, and for all elementary moment tensors in the simulated dataset. The lowest error for each metric is indicated in bold font.

Gabriel Mountains (Fig. 6).

When examining the seismograms that are recorded by individual receivers, we can inspect the amplitudes and timing of the seismic waves directly. We picked out sixteen evenly spaced receivers at the surface of the domain and plotted the velocity time series for the three components of the wavefield (Fig. 7). The locations of the sixteen receivers are indicated in the top left panel of Fig. 5. We also computed the Fourier transforms of the velocity timeseries for each component and plot the spectral amplitudes as a function of frequency ( $\hat{u}(f)$ ,  $\hat{v}(f)$ , and  $\hat{w}(f)$ ) from 0.01 Hz to 1.0 Hz. Note that the time series are lowpass filtered at 0.5 Hz which explains the rapid decay in spectral amplitudes starting around that frequency.

The seismograms and Fourier spectra show good agreement, with the FOM and ROM curves almost always plotting nearly exactly on top of each other. All of the wiggles in the FOM velocity time series are also present in the ROM time series, showing that the ROM reproduces the entire wavefield and accurately captures the duration of ground shaking. The Fourier spectra also show how the amplitudes of the spectral content is very similar between the FOM and ROM. The spectra for some receivers show troughs or peaks in spectral amplitude at narrow frequency bands, and these are also accurately reproduced by the ROM.

### 3.3 ROM ground motion estimates for general point source moment tensor sources

In addition to the six elementary moment tensors ( $\widehat{\mathbf{M}}_1$  through  $\widehat{\mathbf{M}}_6$ ), the ROM and FOM can be used to produce waveforms for general moment tensors expressed as a combination of the six elementary tensors. As



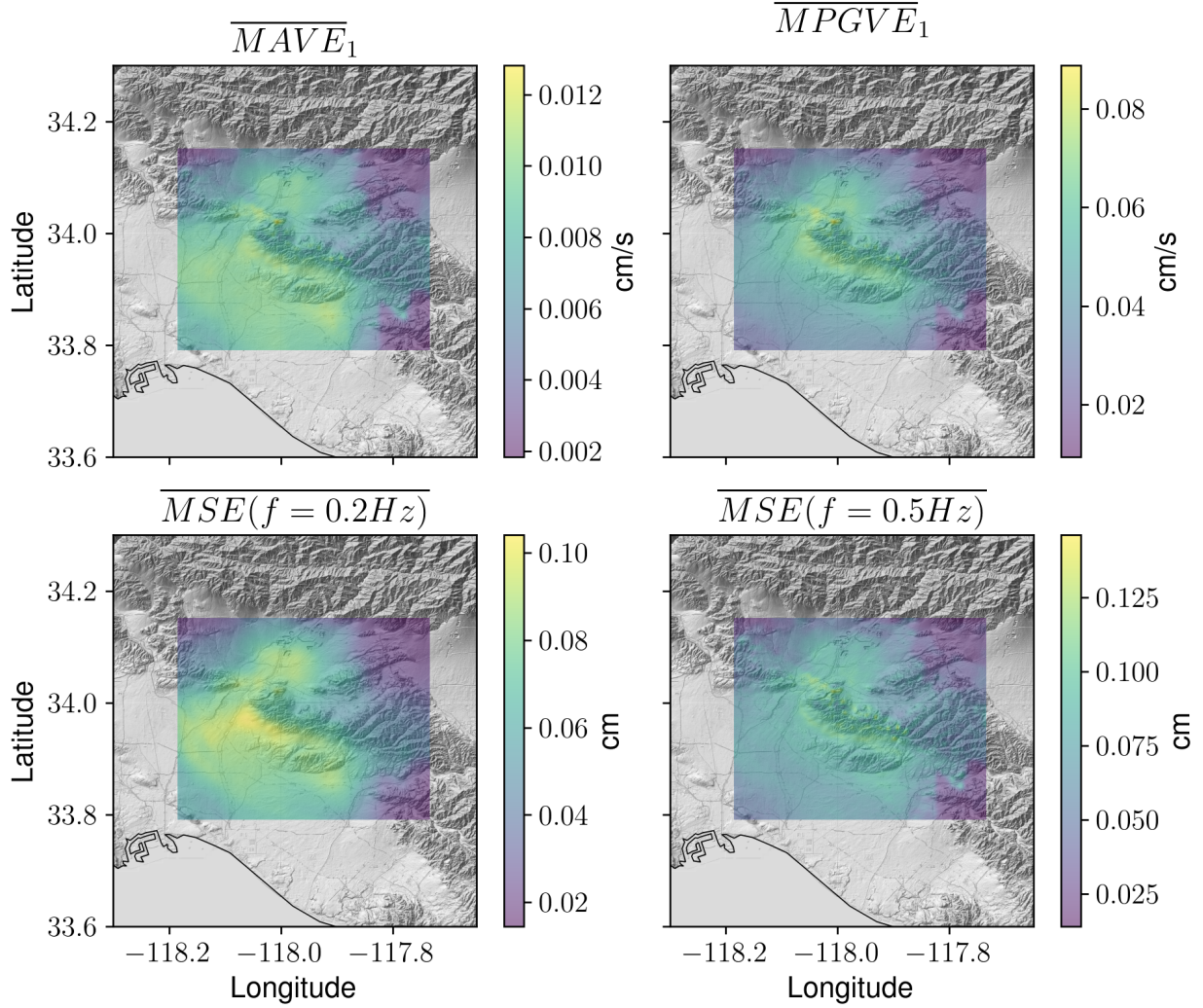


Figure 6: Map views of the leave-one-out ROM mean absolute velocity error (MAVE), mean peak ground velocity error (MPGVE), and mean spectral error (MSE). The errors are averaged over all elementary moment tensor sources in the dataset, and are shown for the east ( $u$ ) component of the surface wavefield. The errors are plotted on top of the topography in southern California and the amplitudes correspond to an  $M_W = 5.0$  earthquake.

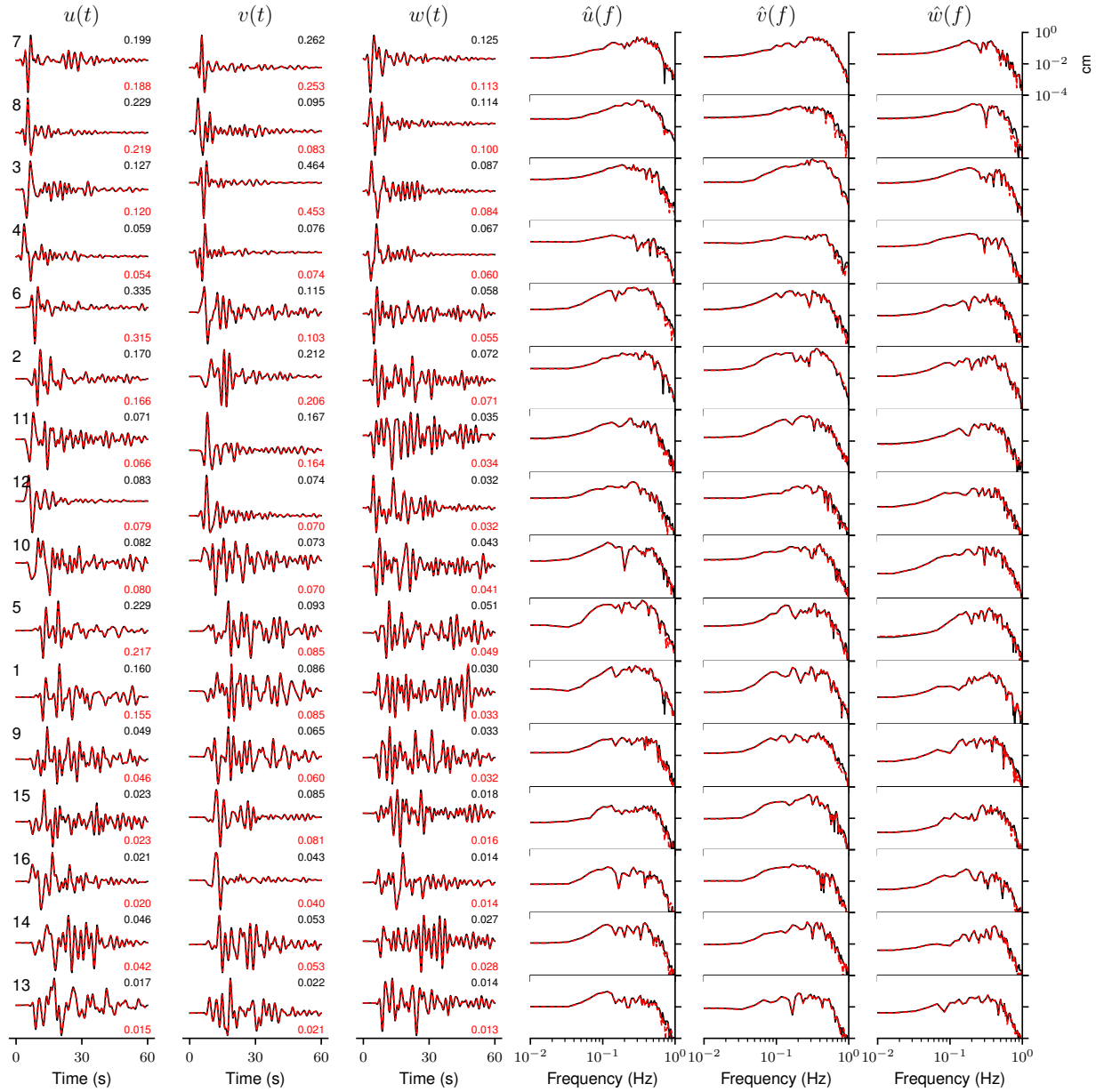


Figure 7: Three-component velocity waveforms ( $u$ ,  $v$ , and  $w$ ) and their Fourier transforms for the sixteen receivers labeled in Fig. 5. The earthquake source is the same as the source for Fig. 5. The FOM data are plotted with a solid black line, and the ROM data with a dashed red line. The receivers are ordered by increasing epicentral distance. The numbers on the right side of the waveform panels indicate maximum absolute value of the waveforms (FOM in black, ROM in red).



a demonstrator, this section focuses on a particular seismic moment tensor given by

$$\bar{\mathbf{M}} = \begin{bmatrix} 0.56 & 1.87 & 2.63 \\ 1.87 & 3.11 & 1.69 \\ 2.63 & 1.69 & -3.67 \end{bmatrix} \times 10^{14} \text{ N m} \quad (29)$$

and located at ( $\Delta\ell = 11.2$  km,  $\Delta w = 4.9$  km,  $\Delta z = 12.0$  km) which is not part of the training dataset. We chose this moment tensor as it corresponds to the first subfault in a finite fault rupture model that we analyze in Sec. 3.4. Upon decomposition into the Kikuchi & Kanamori (1991) basis, we find the following weights

$$\begin{aligned} c_1 &= 1.87, \\ c_2 &= -3.11, \\ c_3 &= 1.69, \\ c_4 &= 2.63, \\ c_5 &= -3.67, \\ c_6 &= 0. \end{aligned}$$

We can use these weights to construct the seismograms for this moment tensor by plugging them into Eq. (16). Since the ROM must be evaluated five times (not six, since  $c_6 = 0$ ), it takes about five times more computing time to obtain the full wavefield solutions for this seismic source, compared to the elementary moment tensor sources in Sec. 3.2.

Similar to the elementary moment tensor source, we plot the map-views of the seismic wavefields (Fig. 8) and the velocity timeseries and Fourier spectra recorded at the same sixteen receivers (Fig. 9). Note that this source is at a slightly different location and depth than the source for Figs. 5 and 7. Despite this change in source, the FOM and ROM wavefields still match well, with differences in velocity less than 0.05 cm/s. Similar to the  $\widehat{\mathbf{M}}_1$  source results, the maximum absolute velocities tend to be slightly under-predicted at worst by about 0.05 cm/s in the epicentral region. The higher frequency 0.5 Hz spectra are also slightly under-predicted in the same area.

Despite small discrepancies, these results instill confidence in our procedure for combining the solutions for different elementary moment tensors. They demonstrate that the errors are not significantly larger for general moment tensors compared to the elementary moment tensors.

### 3.4 ROM ground motion estimates for finite sources

For moderate to large magnitude earthquakes, the point source approximation is often inaccurate for predicting ground motions. Larger earthquakes are typically better modeled as slip distributed on a finite fault

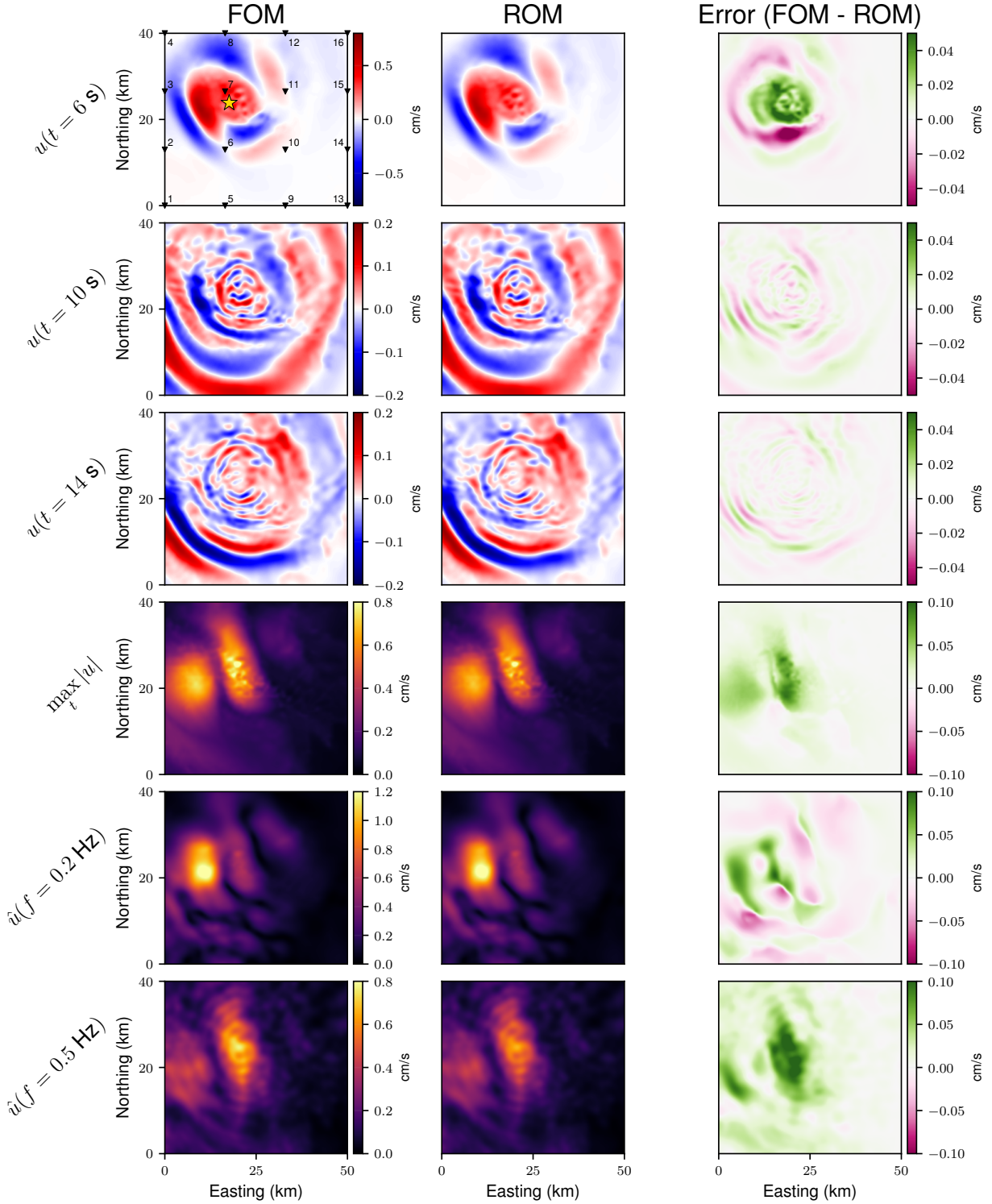


Figure 8: Wavefield snapshots and ground motion intensities, comparing the FOM against the ROM, for a general moment tensor. The figure format is the same as Fig. 5, but is for a different moment tensor source given in Eq. (29). The source location is indicated by the gold star in the top left panel, has a depth of 12.0 km, and a moment magnitude of 5.0. An animated movie of the FOM and ROM velocity wavefields showing all time steps is provided in the supplementary Movie S2.

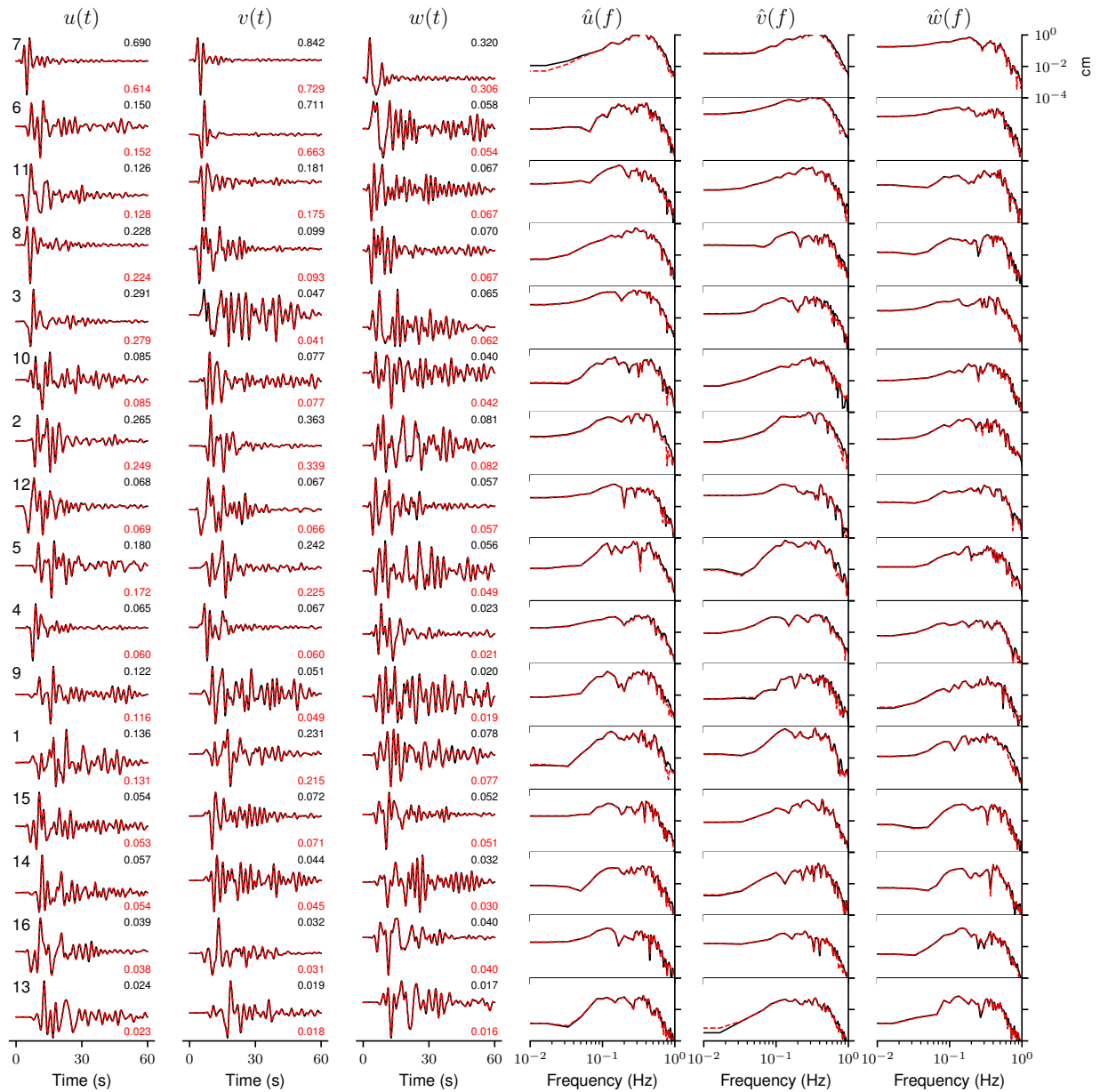


Figure 9: Three-component velocity waveforms ( $u$ ,  $v$ , and  $w$ ) and their Fourier transforms for the same moment tensor source shown in Figure 8. The FOM data are plotted with a solid black line, and the ROM data with a dashed red line. The numbers on the right side of the waveform panels indicate maximum absolute value of the waveforms (FOM in black, ROM in red).

plane (e.g., Ide, 2007; Hayes, 2017). These types of earthquake rupture models can also account for the rupture speed and direction of rupture propagation by modeling the source time function for a set of discrete points on the fault. Accounting for the finite source effects such as rupture directivity can strongly influence ground motion and cause strong asymmetry of the ground motion amplitudes (e.g., Spudich & Chiou, 2008).

As a demonstration example of using our ROMs to predict ground motions for larger magnitude earthquakes, we simulate seismic ground motions for a published kinematic rupture model of the 1987  $M_W$  5.9 Whittier Narrows earthquake. This blind thrust earthquake is now believed to have occurred as part of the Puente Hills thrust system (Shaw et al., 2002) which is situated under the Los Angeles metropolitan area and poses a significant risk to the region (Field et al., 2005). Hartzell & Iida (1990) modeled the earthquake using a kinematic source description, and we use their information on model parameterization that is available from the SRCMOD database (Mai & Thingbaijam, 2014). Their rupture model is parameterized by 100 subfaults that create a square fault with a side length of 10 km. The fault is modeled using a strike of 280 degrees and a dip of 30 degrees. See Fig. 1 for the location of the finite fault in our modeling area. The total slip amplitudes are available from the SRCMOD database, but not the variable dip-slip and strike-slip components. We calculate the dip-slip and strike-slip components by assuming a uniform rake angle of  $58^\circ$  following the focal mechanism solution produced by the Southern California Seismic Network (Hutton et al., 2010).

Hartzell & Iida (1990) developed a few different slip models for this earthquake, using the same parameterization. We specifically use their “L18” model which is available from the SRCMOD database (Mai & Thingbaijam, 2014). The slip distribution for this model is plotted in Fig. 10. This model assumes a constant rupture velocity, starting from the hypocenter, and allows each subfault to rupture twice. The source-time function for each subfault contains two triangular pulses, each with a 0.2 s duration and a time separation of 0.2 s (Fig. 10). We converted this kinematic rupture model into the Standard Rupture Format (Graves, 2014) and then performed a kinematic SeisSol simulation to obtain the seismograms using the FOM procedure described in Sec. 3.4.

To obtain the ROM seismograms, we use the approximate Green’s function and discrete representation theorem, using Eqs. (24) and (25). For this simulation, we must obtain the ROM seismograms using the representation theorem approach as the source time function used by Hartzell & Iida (1990) is different from the source time function,  $\dot{M}(t) = \frac{M_0 t}{T^2}$ , that we used at the 500 discrete training locations.

The FOM and ROM wavefields match well for this finite fault rupture simulation (Fig. 11). The error between the FOM and the ROM velocity amplitudes tends to be no larger than 5% across all time-steps in the simulation. This result is comparable to the results for the general point source moment tensor where the error in the velocity wavefields was also approximately 5% at worst. This result is somewhat surprising given that the finite source uses a significantly more complex rupture model that has many point sources each with a different source time function.

In our finite fault model results, the ROM tends to slightly over-predict the ground motion amplitudes

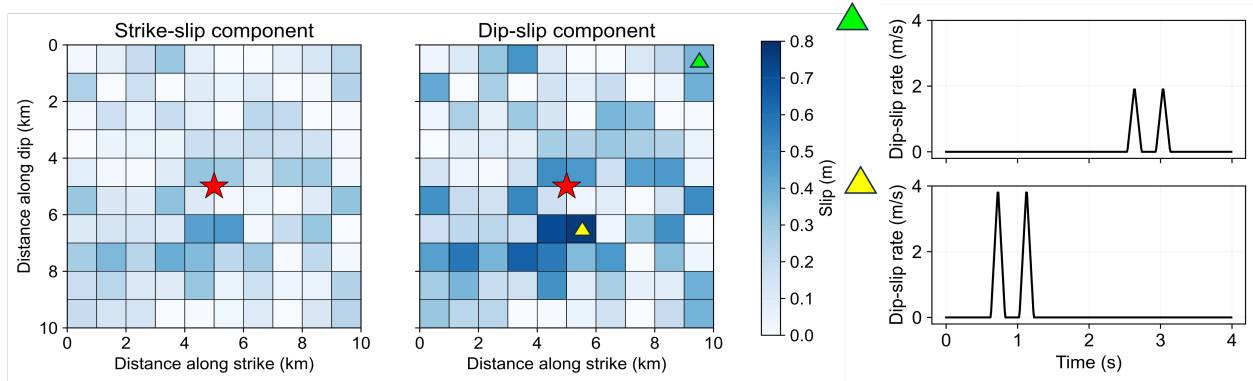


Figure 10: Finite fault model for the 1987  $M_W$  5.9 Whittier Narrows earthquake described in [Hartzell & Iida \(1990\)](#). The images show the strike-slip component, dip-slip component, and slip rate time histories for two of the subfaults in the model.

as seen by the mostly pink colors in the error panel for  $\max_t |u|$ . This might be related to the low-frequency Fourier spectra being over-predicted by the ROM, as the 0.2 Hz panel shows only over-prediction, while the 0.5 Hz panel shows both over- and under-prediction. In the velocity seismograms and Fourier spectra (Fig. 12), the FOM and ROM also show good agreement. As noticed in the wavefields, the ROM absolute maximum velocities tend to be slightly larger than the FOM values. This over-prediction is only at worst about a few cm/s, as seen in receiver number 7 located directly above the fault where the over-prediction is about 3 cm/s.

Obtaining the ROM seismograms for the finite fault simulation requires significantly more computational resources than the point source simulations. The cost of the ROM solutions for finite fault sources scales approximately linearly with the number of subfaults, if we assume one general moment tensor source representing each subfault in the FOM, as the finite fault runtime (0.71 CPUh) is about 100 times the runtime of the general moment tensor source (0.0067 CPUh). This finite fault runtime also includes the time spent computing the Green’s functions, multiplication in the frequency domain, and computing the inverse Fourier transforms, which explains why the scaling is not perfectly linear. Despite this additional cost, the ROM is still two orders magnitude faster than the FOM. However, if more than 100 moment tensor point sources are used to represent the kinematic model, then the computational speedup achieved by using the ROM would be smaller. See Table 2 for the full list of runtimes and speedups for the FOM and ROM for different source descriptions.

### 3.5 Real data comparison for a Los Angeles area earthquake

To demonstrate using our ROM for simulating real earthquakes, we selected an earthquake in the Los Angeles area with USGS event ID ci10399801. This was an  $M_W$  3.55 earthquake that occurred in 2009 with a depth of 5.0 km and was located towards near the southeast corner of our source region (Fig. 13). This earthquake

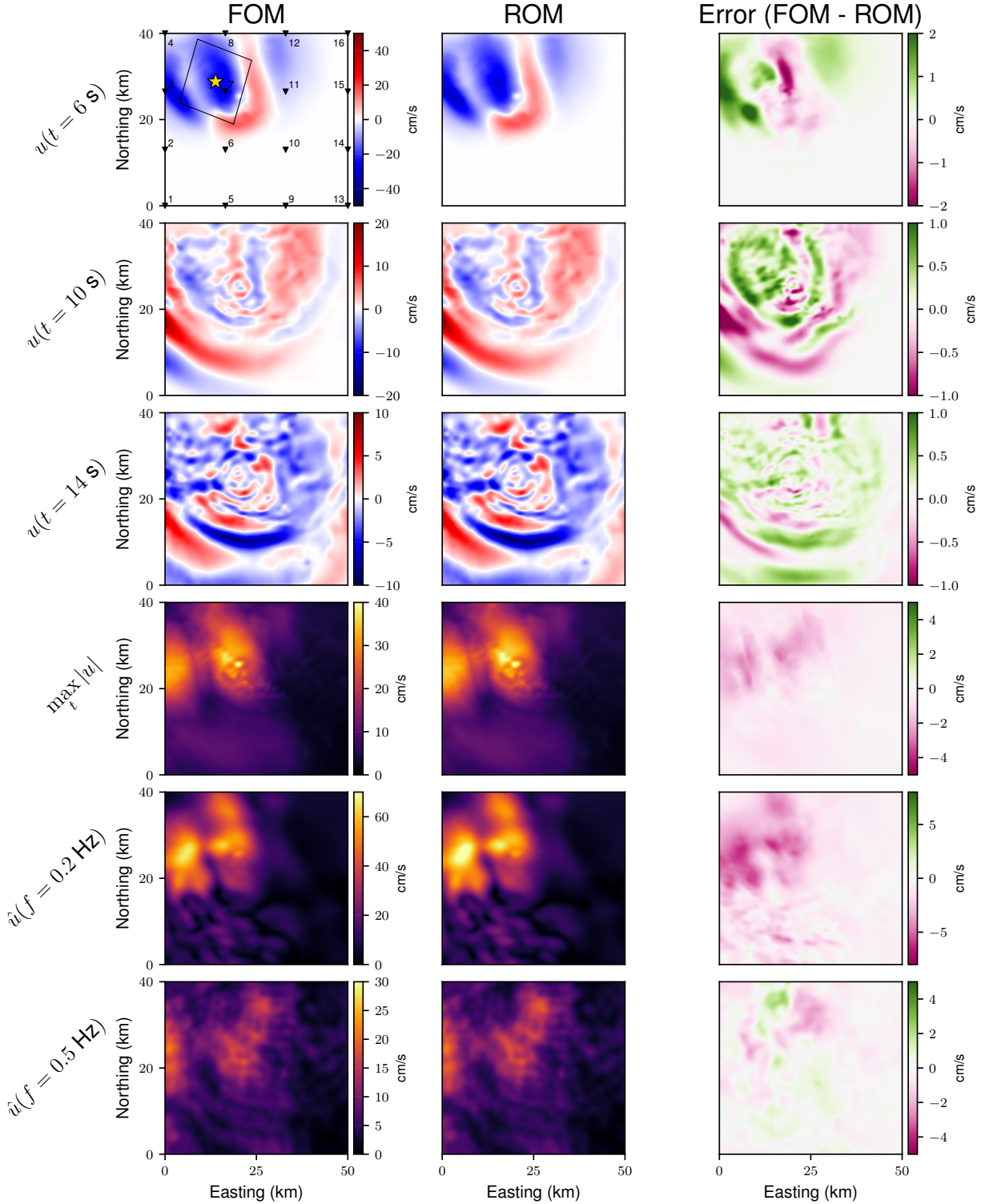


Figure 11: Wavefield snapshots and ground motion intensities, comparing the FOM against the ROM for the 1987  $M_W$  5.9 Whittier Narrows finite fault simulation. The source model is the “L18” kinematic rupture model from [Hartzell & Iida \(1990\)](#). The rupture extent of the finite fault is outlined by the black rectangle in the top left panel. An animated movie of the FOM and ROM velocity wavefields showing all time steps is provided in the supplementary Movie S3.



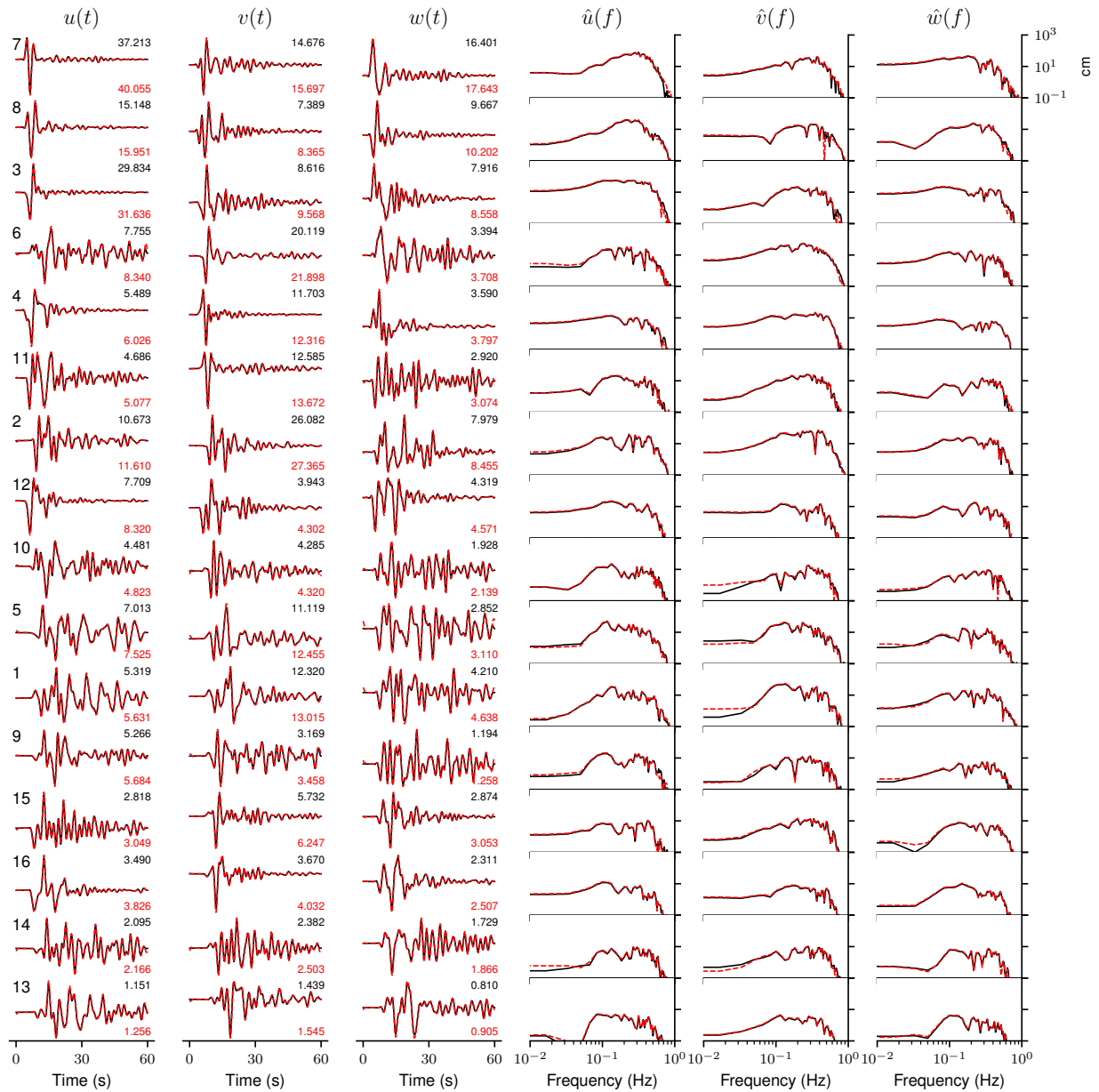


Figure 12: Three-component velocity waveforms ( $u$ ,  $v$ , and  $w$ ) and their Fourier transforms for the Whittier Narrows finite fault source. The FOM data are plotted with a solid black line, and the ROM data with a dashed red line. The numbers on the right side of the waveform panels indicate maximum absolute value of the waveforms (FOM in black, ROM in red).

	FOM (CPUh)	ROM (CPUh)	Speedup
Single elementary tensor	192	0.0011	1.75E+05
General moment tensor (6 components)	192	0.0067	2.87E+04
Finite fault (100 sub-faults)	198	0.7101	2.79E+02

Table 2: FOM and ROM runtimes. The numbers indicate the CPUh usage required to generate the complete 60-second, three-component velocity waveforms for all 8,181 receivers. The ROM value for the single elementary tensor indicates the time spent performing the summation of the POD basis using Eq. (15). The general moment tensor row indicates the time spent solving for the elementary moment tensor weights in Eq. (6) and summing the six-component POD basis (Eq. (16)). The ROM time for the finite fault includes the time to calculate elementary weights in Eq. (6), compute seismograms using Eq. (16), compute approximate Green’s function using Eq. (24), and perform the convolution and summation in Eq. (25). The speedup is calculated by dividing the FOM column by the ROM column. The time spent computing the SVD is not included in the ROM runtimes. We measured the SVD time to be approximately 87 seconds on a single core on SuperMUC-NG using an Intel Skylake Xeon Platinum 8174 processor and a single thread. The SVD time decreased to about  $\approx 20$  seconds when using 16 threads.

was included in the simulations performed by [Lai et al. \(2020\)](#) who also used CVM-S4.26.M01 and found good agreement between real and simulated data on the tangential velocity component at station CI.BRE, the Southern California Edison Barre Peaker power station in Stanton, CA. This recording exhibits strong amplification due to the Los Angeles Basin. We obtained the recorded velocity data from the broadband seismometer at station CI.BRE from the Southern California Earthquake Data Center ([SCEDC, 2013](#)) and processed the data by removing the mean, removing the response, bandpass filtering from 5-10 seconds, and rotating to the tangential component. To obtain the ROM velocity data, we used the Southern California Seismic Network moment tensor solution ([Hutton et al., 2010](#)) and Eq. (16) to obtain the predicted velocity data. We then selected the receiver that was located nearest to station CI.BRE. The bandpass filtered velocity data show good agreement, as the timing and amplitudes on the tangential component match well between the ROM and observed data (Fig. 13).



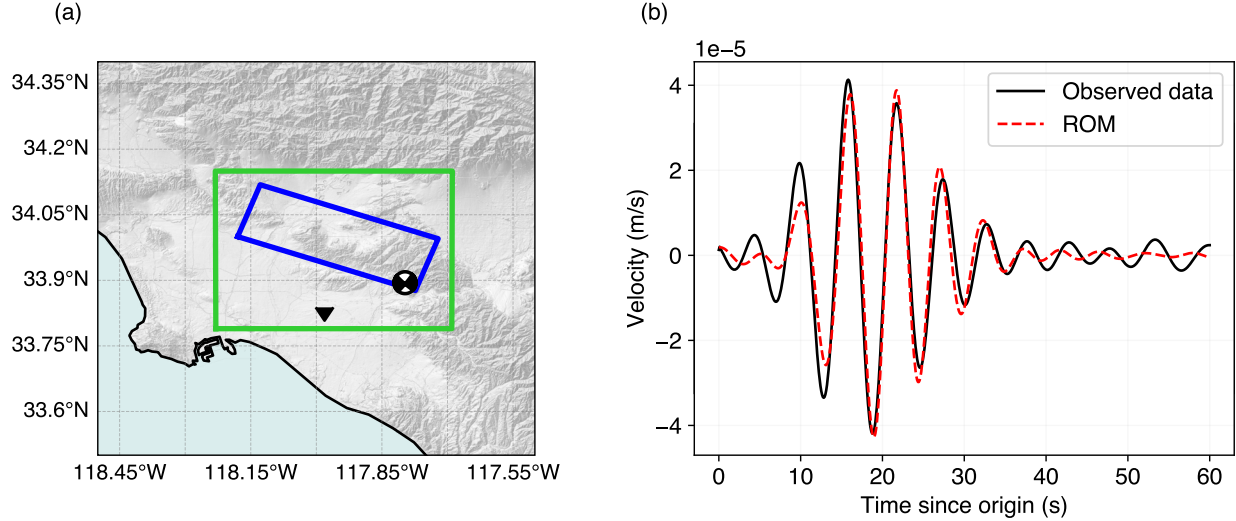


Figure 13: (a) Location of a real earthquake (USGS event ID ci10399801) that occurred in 2009 and the station CLBRE we used to validate the ROM with real data. The earthquake moment magnitude is 3.55 and the depth is 5.0 km. We use the moment tensor solution produced by the Southern California Seismic Network (Hutton et al., 2010). (b) We plot the tangential component of the velocity, in solid black, using the data from the broadband seismometer at station CLBRE. We processed the data by removing the mean, removing the instrument response, bandpass filtering from 5-10 seconds following Lai et al. (2020), and rotating to obtain the tangential component. We also plot the filtered ROM velocity data for the tangential component, in dashed red, at the nearest receiver for this moment tensor solution.

## 4 Discussion

### 4.1 Comparison with Previous Work

This work demonstrates that simulated seismic wavefields can be accurately approximated using a non-intrusive reduced-order model to obtain rapid solutions for earthquakes described by moment tensor point sources or finite slip models in a region of southern California. This work significantly extends the ROMs presented in Rekoske et al. (2023) which generate PGVs, rather than complete waveforms, for only a single epicentral location. We show that our time-dependent approach is applicable to finite sources by exploiting superposition of the wave equation.

The field of using machine learning or other interpolation approaches for simulating seismic wave propagation is rapidly advancing (e.g., Yang et al., 2021, 2023; Lehmann et al., 2024). However, direct one-to-one comparison with our work is challenging, especially in terms of accuracy and computational cost. Several methods have demonstrated rapid seismic waveform modeling in 2D (Moseley et al., 2020; Rasht-Behesht et al., 2022; Yang et al., 2021, 2023), but rapid 3D seismic wave propagation is more challenging. Some

of the recently proposed approaches using 3D wave propagation simulations develop methods for complete 3D wavefields (Kong & Rodgers, 2023; Zou et al., 2023) while others predict 2D wavefields at the surface (Lehmann et al., 2024; Li et al., 2023a). Lehmann et al. (2024) used a factorized Fourier neural operator to simulate surface wavefields for a family of 3D velocity models and reported a relative RMSE of 17% for point sources. Due to the many choices involved in simulating seismic wave propagation, it is difficult to directly compare results head-to-head. Some of these choices include: (1) the resolved frequency band, (2) the constitutive law (i.e., acoustic, elastic, or visco-elastic), (3) the dimension (i.e., 2D or 3D) and size of the simulation domain, (4) the spatial heterogeneities due to velocity model, attenuation, and topography, and (5) the spatial and temporal resolution of the surface wavefields. Comparing with Lehmann et al. (2024), we note that the maximum frequency resolved in our seismograms is lower (e.g., 0.5 Hz compared to 5 Hz), though our wavefield area is larger (2000 km<sup>2</sup> compared to  $\sim$ 100 km<sup>2</sup>), the duration of our seismograms is longer (60 s compared to 7 s), and we include more receivers (8181 compared to 256). Despite the lower frequency we resolve, our FOMs are more computationally expensive ( $\approx$ 200 CPUh vs.  $\approx$ 20 CPUh) as we model a larger area and slower wavespeeds (500 m/s vs.  $\sim$ 1000 m/s) and account for visco-elastic attenuation, which adds  $\approx$ 80% computational cost when using SeisSol (Uphoff & Bader, 2016) but may increase computational cost differently using other implementations. Given that our realistic model setup includes topography and slow wavespeeds, and our small average error of 0.007 cm/s for an  $M_W$  5.0 earthquake, we think that our ROM approach offers an advantage when a preferred, single velocity model is chosen for wavefield prediction; neural operators may offer better generalizability when using families of velocity models or performing seismic tomography.

One advantage of using RBFs for interpolating the POD coefficients in our work is that LOOCV errors can be computed at very little computational expense. When using large neural networks, computing LOOCV errors would typically require an expensive retraining procedure, such that errors are usually reported for only one train/test split instance. The LOOCV errors we present here are conservative estimates of the true ROM error, i.e., the errors in real-time application of the ROM for new unseen earthquakes would likely be lower due to the smaller average spacing between sources (Fig. 14). For any one of the training source locations, the average distance to the nearest neighboring source location  $d_{nearest}$  is 1.80 km; for any earthquake that might occur in the entire volume described by  $\mathcal{P}$  the average  $d_{nearest}$  is slightly smaller at 1.42 km (Fig. 14). In contrast to LOOCV, relying on a single test/train split provides just one estimate of model performance, and the evaluation might not reflect the true performance of the model on unseen data.

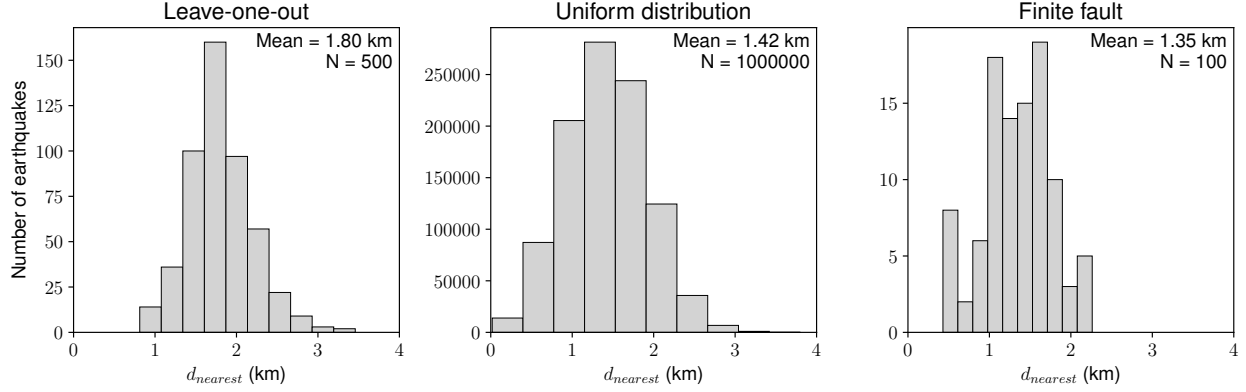


Figure 14: Histograms showing the distribution of  $d_{nearest}$  for three different datasets. The left panel shows the histogram for the Halton sequence used for performing the leave-one-out cross validation to determine the ROM accuracy. The middle panel shows the distribution for a uniform distribution in the parameter space that contains  $10^6$  source locations. The right panel shows the distribution for the source locations in the Whittier Narrows finite fault model.

Our study also provides a new perspective on the efficient use of numerically calculated elastodynamic Green’s functions. Previous work using interpolated Green’s functions is also typically based on reciprocal simulations (e.g., Wang & Zhan, 2020). Others have suggested that for applications using multi-linear interpolation of numerically precomputed Green’s functions, their spacing should be no greater than a quarter of the minimum wavelength (Heimann et al., 2019). The minimum wavelength is calculated by dividing the minimum wave velocity by the maximum frequency. In our 0.5 Hz accurate FOM forward simulations with  $V_{S,min} = 500$  m/s, the minimum wavelength is 1 km, which would require a minimum spacing of Green’s functions of 250 m for accurate multilinear interpolation. Our results (e.g., Figs. 5 and 7) suggest that a Green’s function spacing even as large as about 2 km, which is nearly twice the minimum wavelength, is sufficient to produce accurate ROM interpolations when using interpolated POD with RBFs. Other work suggests that it is superior to interpolate Green’s functions using the frequency-wavenumber domain (Gülünay, 2003), though a thorough comparison between interpolation methods in various domains is outside the scope of this paper. Future work may investigate other spectral decompositions, manifold interpolation, or shifted proper orthogonal decomposition to better decompose advection-dominated wave equations (e.g., Reiss et al., 2018; Lu & Tartakovsky, 2020).

## 4.2 Limitations

One limitation in our study relates to limited resolution we chose for the forward simulations, as the maximum frequency content in our seismograms of 0.5 Hz is lower than required for most engineering applications. We do not interpolate the waveforms in time, meaning that the ROM always generates 60-second waveforms sampled at 10 Hz. However, this is not a disadvantage of the ROM approach but merely a choice we

made to limit our simulation computational costs; higher resolution forward simulations would readily allow extending our ROM approach to higher frequencies. A true disadvantage of this ROM approach is that predicting the seismic wavefields for a different velocity model is not easily possible. For example, several alternative 3D velocity models are available for this region that we could have used, such as CVM-H or CVM-S, and it would be interesting to apply our ROMs to different regions such as northern California or Cascadia. However, with the current approach, as many new, expensive simulations would be required for each velocity model.

We note that the complex issue of nonlinearities in ground motion prediction is a substantial consideration, especially for large earthquakes (e.g., [Field et al., 1997](#); [Rubinstein & Beroza, 2004](#); [Roten et al., 2014](#)). At this time, our FOM simulations do not account for soil nonlinearity or off-fault plasticity which may influence the strength of ground motions. Our approach for simulating large earthquakes by the summation of point sources would not be applicable for nonlinear wavefield effects, as the linear superposition of seismic sources would be broken in the nonlinear case. Additional work or methods are needed to consider how to rapidly obtain physics-based simulation results that would consider nonlinear source or wavefield effects for which the principle of superposition of the wave equation is no longer valid.

### 4.3 Future work and implications

One advantage of predicting complete timeseries data instead of individual ground motion metrics is that any ground motion metrics can be computed from the timeseries data. We focused on a few select metrics, such as the MPGVE and MSE, that could be relevant for earthquake early warning and seismic hazard applications. However, if new ground motion metrics become standard in the engineering community, then those can be computed using the same FOM data. Another improvement in the present study is that we allow for varying epicentral locations and moment tensors. This feature allows one to compute accurate wavefields for sources distributed throughout the whole volume, not just for a set of assumed faults. This is especially important in an area such as the Los Angeles Basin which is known for having blind thrust earthquakes on faults that were only identified after they had caused significant damage (e.g., [Shaw et al., 2002](#)).

Given the accuracy and speed of our ROMs compared to the simulations, we speculate that ROMs could complement empirical ground motion models used for probabilistic seismic hazard analysis (PSHA) and earthquake early warning (EEW). Recent earthquake simulations using southern California community velocity and attenuation models, e.g., CVM-H ([Süss & Shaw, 2003](#)) and CVM-S ([Magistrale et al., 1996](#)), can achieve good agreement with real data, especially at longer periods ([Lai et al., 2020](#)). For example, simulations by [Hu et al. \(2022\)](#) suggest standard deviations of about 0.3 natural log units for 0.5 Hz Fourier amplitude spectra data, compared to the [Bayless & Abrahamson \(2019\)](#) GMM for California which reports a total standard deviation of 0.75 natural log units. This suggests that our ROMs using southern California velocity models should also achieve an adequate match with data for real earthquakes. That said, a limitation

in our approach is that our ROM will not accurately extrapolate for sources located outside the box,  $\mathcal{P}$  (see Fig. 1 and Fig 2). Assuming a land area of 403,932 km<sup>2</sup> representing the state of California, generating simulation data for 2-km spaced sources for a volume of the entire state would require about 800,000 point source locations. This means the total upfront computational cost would be  $800,000 \times 6 \times 192$  CPUh = 921.6 million CPUh. We expect that the approach in this paper should apply for other areas that have 3D velocity models, such as the San Francisco Bay Area (e.g., Hole et al., 2000) or the Cascadia subduction zone (Stephenson et al., 2017). Further validation by comparing ROMs against ground motions recorded from real earthquakes would support supplementing GMM predictions with physics-informed ROM predictions in real-time earthquake alerts, though we save this validation for future work. We note that applying these ROMs for source-based EEW (e.g., Böse et al., 2018; Chung et al., 2019) would also require determining a rapid focal mechanism solution and hypocentral depth.

For PSHA, our method allows us to obtain a surface seismic wavefield with high spatial resolution because the method does not use reciprocity. In comparison, the CyberShake framework (e.g., Graves et al., 2011) uses the reciprocity property of the wave equation as they evaluate suites of seismic timeseries for many different earthquake scenarios, but a relatively limited number of sites. CyberShake then constructs probabilistic seismic hazard maps by spatial interpolation of the site terms. Thus, CyberShake simulations computationally scale with the number of sites (generally on the order of hundreds), and not with the total number of potential earthquake scenarios (usually on the order of tens to hundreds of thousands of finite fault sources). To generate wavefields with high spatial resolution with CyberShake, more sites would need to be added and the computational cost would greatly increase. However, with the ROM approach based on forward simulations, adding more sites adds a negligible cost to the FOM simulations provided that the domain size is unchanged; evaluating the ROM will become slightly more expensive with each additional site due to the larger matrices that must be multiplied together in Eq. 15. However, by using this advantage, we speculate that ROMs could improve the spatial resolution of probabilistic seismic hazard maps without drastically increasing the computational requirements.

## 5 Conclusion

In conclusion, our study demonstrates the potential of using reduced-order models to rapidly and accurately generate physics-based seismic wavefields. The method is based on interpolated proper orthogonal decomposition using radial basis functions, and generates three-component, velocity seismograms based on 3D wave propagation simulations using a 3D seismic velocity model for southern California. We find that the ROM approach offers a significant improvement in computational efficiency, likely making it fast enough for real-time applications in earthquake early warning and seismic hazard assessment. Our method is also quite modular, in that it can be applied for single general moment tensors as well as complex finite fault rupture models composed of multiple subfaults with heterogeneous slip distributions and varying source time

functions. The speedup for elementary moment tensors is on the order of  $10^5$ , and on the order of  $10^2$  for a finite fault rupture model consisting of 100 subfaults. For an  $M_W$  5.0 earthquake, the mean absolute error in the velocity seismograms is about 0.007 cm/s for the horizontal components, and 0.004 cm/s for the vertical component. These results confirm the feasibility of using ROMs to approximate complex seismic wave dynamics with high fidelity. Our results also provide a new perspective on the interpolation of elastodynamic Green’s functions, suggesting that accurate interpolations can be obtained when the source-to-source distance is up to  $\approx 2$  times the shortest wavelength. This study shows progress towards providing rapid and accurate Green’s functions that might be used in future real-time applications and source inversions.

## Acknowledgements

We thank Wenyuan Fan for suggesting the usage of the moment tensor decomposition from [Kikuchi & Kanamori \(1991\)](#). JMR acknowledges support from the National Science Foundation Graduate Research Fellowship Program (grant No. DGE-2038238). DAM and AAG were supported by the National Science Foundation through grant Nos. EAR-2121568 and OAC-2311208. Any opinions, findings, and conclusions or recommendations expressed in this material are those of the author(s) and do not necessarily reflect the views of the National Science Foundation. We gratefully acknowledge the Gauss Center for Supercomputing e.V. ([www.gauss-centre.eu](http://www.gauss-centre.eu)) for providing compute time on SuperMUC-NG, hosted at the Leibniz Supercomputing Center ([www.lrz.de](http://www.lrz.de)), via project pn49ha.

## References

- Abercrombie, R. E., 2015. Investigating uncertainties in empirical Green’s function analysis of earthquake source parameters, *Journal of Geophysical Research: Solid Earth*, **120**(6), 4263–4277.
- Abrahamson, N. A., Silva, W. J., & Kamai, R., 2014. Summary of the ASK14 ground motion relation for active crustal regions, *Earthquake Spectra*, **30**(3), 1025–1055.
- Aki, K. & Richards, P. G., 2002. *Quantitative Seismology*, University Science Books.
- Audouze, C., De Vuyst, F., & Nair, P., 2009. Reduced-order modeling of parameterized PDEs using time–space-parameter principal component analysis, *International journal for numerical methods in engineering*, **80**(8), 1025–1057.
- Bayless, J. & Abrahamson, N. A., 2019. Summary of the BA18 ground-motion model for Fourier amplitude spectra for crustal earthquakes in California, *Bulletin of the Seismological Society of America*, **109**(5), 2088–2105.
- Benner, P., Gugercin, S., & Willcox, K., 2015. A survey of projection-based model reduction methods for parametric dynamical systems, *SIAM review*, **57**(4), 483–531.

- Berkooz, G., Holmes, P., & Lumley, J. L., 1993. The proper orthogonal decomposition in the analysis of turbulent flows, *Annual review of fluid mechanics*, **25**(1), 539–575.
- Boore, D. M., Stewart, J. P., Seyhan, E., & Atkinson, G. M., 2014. NGA-West2 equations for predicting PGA, PGV, and 5% damped PSA for shallow crustal earthquakes, *Earthquake Spectra*, **30**(3), 1057–1085.
- Böse, M., Heaton, T. H., & Hauksson, E., 2012. Real-time finite fault rupture detector (FinDer) for large earthquakes, *Geophysical Journal International*, **191**(2), 803–812.
- Böse, M., Smith, D. E., Felizardo, C., Meier, M.-A., Heaton, T. H., & Clinton, J. F., 2018. Finder v. 2: Improved real-time ground-motion predictions for M2–M9 with seismic finite-source characterization, *Geophysical Journal International*, **212**(1), 725–742.
- Breuer, A. & Heinecke, A., 2022. Next-Generation Local Time Stepping for the ADER-DG Finite Element Method, in *2022 IEEE International Parallel and Distributed Processing Symposium (IPDPS)*, pp. 402–413, IEEE Computer Society, Los Alamitos, CA, USA.
- Brune, J. N., 1970. Tectonic stress and the spectra of seismic shear waves from earthquakes, *Journal of geophysical research*, **75**(26), 4997–5009.
- Bui-Thanh, T., Damodaran, M., & Willcox, K., 2003. Proper orthogonal decomposition extensions for parametric applications in compressible aerodynamics, in *21st AIAA applied aerodynamics conference*, p. 4213.
- Campbell, K. W. & Bozorgnia, Y., 2014. NGA-West2 ground motion model for the average horizontal components of PGA, PGV, and 5% damped linear acceleration response spectra, *Earthquake Spectra*, **30**(3), 1087–1115.
- Chaljub, E., Moczo, P., Tsuno, S., Bard, P.-Y., Kristek, J., Käser, M., Stupazzini, M., & Kristekova, M., 2010. Quantitative comparison of four numerical predictions of 3D ground motion in the Grenoble Valley, France, *Bulletin of the Seismological Society of America*, **100**(4), 1427–1455.
- Chiou, B. S.-J. & Youngs, R. R., 2014. Update of the Chiou and Youngs NGA model for the average horizontal component of peak ground motion and response spectra, *Earthquake Spectra*, **30**(3), 1117–1153.
- Chung, A. I., Henson, I., & Allen, R. M., 2019. Optimizing earthquake early warning performance: ElarmS-3, *Seismological Research Letters*, **90**(2A), 727–743.
- Crowell, B. W., Bock, Y., & Melgar, D., 2012. Real-time inversion of GPS data for finite fault modeling and rapid hazard assessment, *Geophysical Research Letters*, **39**(9).
- Cui, Y., Olsen, K. B., Jordan, T. H., Lee, K., Zhou, J., Small, P., Roten, D., Ely, G., Panda, D. K., Chourasia, A., et al., 2010. Scalable earthquake simulation on petascale supercomputers, in *SC'10: Proceedings of the*

- 2010 ACM/IEEE International Conference for High Performance Computing, Networking, Storage and Analysis, pp. 1–20, IEEE.
- Dreger, D., 1994. Empirical Green’s function study of the January 17, 1994 Northridge, California earthquake, *Geophysical research letters*, **21**(24), 2633–2636.
- Druault, P., Guibert, P., & Alizon, F., 2005. Use of proper orthogonal decomposition for time interpolation from piv data: Application to the cycle-to-cycle variation analysis of in-cylinder engine flows, *Experiments in fluids*, **39**, 1009–1023.
- Dumbser, M. & Käser, M., 2006. An arbitrary high-order discontinuous Galerkin method for elastic waves on unstructured meshes — II. The three-dimensional isotropic case, *Geophysical Journal International*, **167**(1), 319–336.
- Emmerich, H. & Korn, M., 1987. Incorporation of attenuation into time-domain computations of seismic wave fields, *Geophysics*, **52**(9), 1252–1264.
- Field, E. H., Johnson, P. A., Beresnev, I. A., & Zeng, Y., 1997. Nonlinear ground-motion amplification by sediments during the 1994 Northridge earthquake, *Nature*, **390**(6660), 599–602.
- Field, E. H., Seligson, H. A., Gupta, N., Gupta, V., Jordan, T. H., & Campbell, K. W., 2005. Loss estimates for a Puente Hills blind-thrust earthquake in Los Angeles, California, *Earthquake Spectra*, **21**(2), 329–338.
- Florez, M. A., Caporale, M., Buabthong, P., Ross, Z. E., Asimaki, D., & Meier, M.-A., 2022. Data-driven synthesis of broadband earthquake ground motions using artificial intelligence, *Bulletin of the Seismological Society of America*, **112**(4), 1979–1996.
- Frankel, A., Stephenson, W., & Carver, D., 2009. Sedimentary basin effects in Seattle, Washington: Ground-motion observations and 3D simulations, *Bulletin of the Seismological Society of America*, **99**(3), 1579–1611.
- Fujiwara, H., Kawai, S., Aoi, S., Morikawa, N., Senna, S., Kudo, N., Ooi, M., Hao, K. X.-S., Hayakawa, Y., Toyama, N., et al., 2009. A study on subsurface structure model for deep sedimentary layers of Japan for strong-motion evaluation, *Technical Note of the National Research Institute for Earth Science and Disaster Prevention*, **337**, 260.
- Graves, R., 2014. Standard Rupture Format, Version 2.0, Tech. rep., U.S. Geological Survey, Technical Report.
- Graves, R., Jordan, T. H., Callaghan, S., Deelman, E., Field, E., Juve, G., Kesselman, C., Maechling, P., Mehta, G., Milner, K., et al., 2011. Cybershake: A physics-based seismic hazard model for southern California, *Pure and Applied Geophysics*, **168**, 367–381.



- Gülünay, N., 2003. Seismic trace interpolation in the Fourier transform domain, *Geophysics*, **68**(1), 355–369.
- Hartzell, S. & Iida, M., 1990. Source complexity of the 1987 Whittier Narrows, California, earthquake from the inversion of strong motion records, *Journal of Geophysical Research: Solid Earth*, **95**(B8), 12475–12485.
- Hartzell, S., Meremonte, M., Ramírez-Guzmán, L., & McNamara, D., 2014. Ground motion in the presence of complex topography: Earthquake and ambient noise sources, *Bulletin of the Seismological Society of America*, **104**(1), 451–466.
- Hartzell, S. H., 1978. Earthquake aftershocks as Green’s functions, *Geophysical Research Letters*, **5**(1), 1–4.
- Hauksson, E. & Jones, L. M., 1988. The 1987 Whittier Narrows earthquake sequence in Los Angeles, southern California: Seismological and tectonic analysis, *Journal of Geophysical Research: Solid Earth*, **93**(B11), 15355–15369.
- Hauksson, E., Yang, W., & Shearer, P. M., 2012. Waveform relocated earthquake catalog for southern California (1981 to June 2011), *Bulletin of the Seismological Society of America*, **102**(5), 2239–2244.
- Hawkins, R., Khalid, M., Smetana, K., & Trampert, J., 2023. Model order reduction for seismic waveform modelling: Inspiration from normal modes, *Geophysical Journal International*, **234**(3), 2255–2283.
- Hayes, G. P., 2017. The finite, kinematic rupture properties of great-sized earthquakes since 1990, *Earth and Planetary Science Letters*, **468**, 94–100.
- Heimann, S., Vasyura-Bathke, H., Sudhaus, H., Isken, M. P., Kriegerowski, M., Steinberg, A., & Dahm, T., 2019. A Python framework for efficient use of pre-computed Green’s functions in seismological and other physical forward and inverse source problems, *Solid Earth*, **10**(6), 1921–1935.
- Heinecke, A., Breuer, A., Rettenberger, S., Bader, M., Gabriel, A.-A., Pelties, C., Bode, A., Barth, W., Liao, X.-K., Vaidyanathan, K., et al., 2014. Petascale high order dynamic rupture earthquake simulations on heterogeneous supercomputers, in *SC’14: Proceedings of the International Conference for High Performance Computing, Networking, Storage and Analysis*, pp. 3–14, IEEE.
- Hesthaven, J. S., Pagliantini, C., & Rozza, G., 2022. Reduced basis methods for time-dependent problems, *Acta Numerica*, **31**, 265–345.
- Hole, J. A., Brocher, T., Klemperer, S., Parsons, T., Benz, H., & Furlong, K., 2000. Three-dimensional seismic velocity structure of the San Francisco Bay area, *Journal of Geophysical Research: Solid Earth*, **105**(B6), 13859–13874.
- Hough, S., 1997. Empirical Green’s function analysis: Taking the next step, *Journal of Geophysical Research: Solid Earth*, **102**(B3), 5369–5384.

- Hough, S. E., 1998. Aftershock sequences as natural experiments for earthquake source models, *Bulletin of the Seismological Society of America*, **88**(4), 1177–1194.
- Hu, Z., Olsen, K. B., & Day, S. M., 2022. 0–5 Hz deterministic 3-D ground motion simulations for the 2014 La Habra, California, Earthquake, *Geophysical Journal International*, **230**(3), 2162–2182.
- Hutton, K., Woessner, J., & Hauksson, E., 2010. Earthquake monitoring in southern California for seventy-seven years (1932–2008), *Bulletin of the Seismological Society of America*, **100**(2), 423–446.
- Ide, S., 2007. 4.07 - Slip Inversion, in *Treatise on Geophysics*, pp. 193–223, ed. Schubert, G., Elsevier, Amsterdam.
- Igel, H., 2017. *Computational Seismology: A Practical Introduction*, Oxford University Press.
- Jordan, T. H. & Callaghan, S., 2018. CyberShake models of seismic hazards in southern and central California, in *Proceedings of the US National Conference on Earthquake Engineering*.
- Käser, M. & Dumbser, M., 2006. An arbitrary high-order discontinuous Galerkin method for elastic waves on unstructured meshes — I. The two-dimensional isotropic case with external source terms, *Geophysical Journal International*, **166**(2), 855–877.
- Käser, M., Dumbser, M., De La Puente, J., & Igel, H., 2007. An arbitrary high-order discontinuous Galerkin method for elastic waves on unstructured meshes—III. Viscoelastic attenuation, *Geophysical Journal International*, **168**(1), 224–242.
- Käser, M., Hermann, V., & de la Puente, J., 2008. Quantitative accuracy analysis of the discontinuous Galerkin method for seismic wave propagation, *Geophysical Journal International*, **173**(3), 990–999.
- Kikuchi, M. & Kanamori, H., 1991. Inversion of complex body waves—III, *Bulletin of the Seismological Society of America*, **81**(6), 2335–2350.
- Koketsu, K., Miyake, H., Fujiwara, H., & Hashimoto, T., 2008. Progress towards a Japan integrated velocity structure model and long-period ground motion hazard map, 14th world conf, *Earthq. Eng., China, Paper ID S10-038*.
- Komatitsch, D. & Tromp, J., 1999. Introduction to the spectral element method for three-dimensional seismic wave propagation, *Geophysical journal international*, **139**(3), 806–822.
- Komatitsch, D. & Vilotte, J.-P., 1998. The spectral element method: an efficient tool to simulate the seismic response of 2D and 3D geological structures, *Bulletin of the seismological society of America*, **88**(2), 368–392.
- Komatitsch, D., Liu, Q., Tromp, J., Suss, P., Stidham, C., & Shaw, J. H., 2004. Simulations of ground motion in the Los Angeles basin based upon the spectral-element method, *Bulletin of the Seismological Society of America*, **94**(1), 187–206.

- Kong, Q. & Rodgers, A., 2023. Feasibility of using fourier neural operators for 3d elastic seismic simulations, Tech. rep., Lawrence Livermore National Laboratory (LLNL), Livermore, CA (United States).
- Kristek, J. & Moczo, P., 2003. Seismic-wave propagation in viscoelastic media with material discontinuities: A 3D fourth-order staggered-grid finite-difference modeling, *Bulletin of the Seismological Society of America*, **93**(5), 2273–2280.
- Kusanovic, D. S., Taborda, R., & Asimaki, D., 2023. Soil–structure interaction effects on a regional scale through ground-motion simulations and reduced order models: A case study from the 2008 Mw 5.4 Chino Hills mainshock, *Bulletin of the Seismological Society of America*, **113**(6), 2557–2573.
- Lai, V. H., Graves, R. W., Yu, C., Zhan, Z., & Helmberger, D. V., 2020. Shallow basin structure and attenuation are key to predicting long shaking duration in Los Angeles basin, *Journal of Geophysical Research: Solid Earth*, **125**(10), e2020JB019663.
- Lazaro, D. & Montefusco, L. B., 2002. Radial basis functions for the multivariate interpolation of large scattered data sets, *Journal of Computational and Applied Mathematics*, **140**(1-2), 521–536.
- Lehmann, F., Gatti, F., Bertin, M., & Clouteau, D., 2024. 3D elastic wave propagation with a factorized Fourier neural operator (F-FNO), *Computer Methods in Applied Mechanics and Engineering*, **420**, 116718.
- Li, C., Ji, D., Zhai, C., Cao, Z., & Ma, Y., 2023a. Rcn: Recurrent convolutional neural network for solving 3d wave equation, *IEEE Geoscience and Remote Sensing Letters*.
- Li, Y., Villa, V., Clayton, R. W., & Persaud, P., 2023b. Shear wave velocities in the San Gabriel and San Bernardino basins, California, *Journal of Geophysical Research: Solid Earth*, **128**(7), e2023JB026488.
- Lin, G., Shearer, P. M., Hauksson, E., & Thurber, C. H., 2007. A three-dimensional crustal seismic velocity model for southern California from a composite event method, *Journal of Geophysical Research: Solid Earth*, **112**(B11).
- Liu, P. & Archuleta, R. J., 2004. A new nonlinear finite fault inversion with three-dimensional Green’s functions: Application to the 1989 Loma Prieta, California, earthquake, *Journal of Geophysical Research: Solid Earth*, **109**(B2).
- Lu, H. & Tartakovsky, D. M., 2020. Lagrangian dynamic mode decomposition for construction of reduced-order models of advection-dominated phenomena, *Journal of Computational Physics*, **407**, 109229.
- Magistrale, H., McLaughlin, K., & Day, S., 1996. A geology-based 3D velocity model of the Los Angeles basin sediments, *Bulletin of the Seismological Society of America*, **86**(4), 1161–1166.
- Magistrale, H., Day, S., Clayton, R. W., & Graves, R., 2000. The SCEC southern California reference three-dimensional seismic velocity model version 2, *Bulletin of the Seismological Society of America*, **90**(6B), S65–S76.

- Mai, P. M. & Thingbaijam, K. K. S., 2014. SRCMOD: An online database of finite-fault rupture models, *Seismological Research Letters*, **85**(6), 1348–1357.
- Marshall, S., Plesch, A., & Shaw, J., 2023. SCEC Community Fault Model (CFM).
- Milner, K. R., Shaw, B. E., Goulet, C. A., Richards-Dinger, K. B., Callaghan, S., Jordan, T. H., Dieterich, J. H., & Field, E. H., 2021. Toward physics-based nonergodic PSHA: A prototype fully deterministic seismic hazard model for southern California, *Bulletin of the Seismological Society of America*, **111**(2), 898–915.
- Minson, S. E., Murray, J. R., Langbein, J. O., & Gomberg, J. S., 2014. Real-time inversions for finite fault slip models and rupture geometry based on high-rate GPS data, *Journal of Geophysical Research: Solid Earth*, **119**(4), 3201–3231.
- Moczo, P., Kristek, J., & Halada, L., 2004. The finite-difference method for seismologists, *An Introduction*, **161**.
- Monterrubio-Velasco, M., Callaghan, S., Modesto, D., Carrasco, J. C., Badia, R. M., Pallares, P., Vázquez-Novoa, F., Quintana-Ortí, E. S., Pienkowska, M., & de la Puente, J., 2024. A machine learning estimator trained on synthetic data for real-time earthquake ground-shaking predictions in southern California, *Communications Earth & Environment*, **5**(1), 258.
- Moschetti, M. P., Churchwell, D., Thompson, E. M., Rekoske, J. M., Wolin, E., & Boyd, O. S., 2021. Seismic wave propagation and basin amplification in the Wasatch Front, Utah, *Seismological Society of America*, **92**(6), 3626–3641.
- Moschetti, M. P., Thompson, E. M., & Withers, K., 2024. Basin effects from 3D simulated ground motions in the Greater Los Angeles region for use in seismic hazard analyses, *Earthquake Spectra*, **40**(2), 1042–1065.
- Moseley, B., Nissen-Meyer, T., & Markham, A., 2020. Deep learning for fast simulation of seismic waves in complex media, *Solid Earth*, **11**(4), 1527–1549.
- Murray, J. R., Thompson, E. M., Baltay, A. S., & Minson, S. E., 2022. The impact of 3D finite-fault information on ground-motion forecasting for earthquake early warning, *Bulletin of the Seismological Society of America*, **112**(2), 779–802.
- Nagata, T., Nakai, K., Yamada, K., Saito, Y., Nonomura, T., Kano, M., Ito, S.-i., & Nagao, H., 2023. Seismic wavefield reconstruction based on compressed sensing using data-driven reduced-order model, *Geophysical Journal International*, **233**(1), 33–50.
- Nissen-Meyer, T., van Driel, M., Stähler, S. C., Hosseini, K., Hempel, S., Auer, L., Colombi, A., & Fournier, A., 2014. AxiSEM: Broadband 3-D seismic wavefields in axisymmetric media, *Solid Earth*, **5**(1), 425–445.

- Olsen, K., 2000. Site amplification in the Los Angeles basin from three-dimensional modeling of ground motion, *Bulletin of the Seismological Society of America*, **90**(6B), S77–S94.
- Olsen, K., Day, S., & Bradley, C., 2003. Estimation of  $q$  for long-period ( $> 2$  sec) waves in the Los Angeles basin, *Bulletin of the Seismological Society of America*, **93**(2), 627–638.
- Pereyra, V. & Kaelin, B., 2008. Fast wave propagation by model order reduction, *Electronic Transactions on Numerical Analysis*, **30**, 406–419.
- Rasht-Behesht, M., Huber, C., Shukla, K., & Karniadakis, G. E., 2022. Physics-informed neural networks (PINNs) for wave propagation and full waveform inversions, *Journal of Geophysical Research: Solid Earth*, **127**(5), e2021JB023120.
- Reiss, J., Schulze, P., Sesterhenn, J., & Mehrmann, V., 2018. The shifted proper orthogonal decomposition: A mode decomposition for multiple transport phenomena, *SIAM Journal on Scientific Computing*, **40**(3), A1322–A1344.
- Rekoske, J. M., Moschetti, M. P., & Thompson, E. M., 2022. Basin and site effects in the US Pacific Northwest estimated from small-magnitude earthquakes, *Bulletin of the Seismological Society of America*, **112**(1), 438–456.
- Rekoske, J. M., Gabriel, A.-A., & May, D. A., 2023. Instantaneous physics-based ground motion maps using reduced-order modeling, *Journal of Geophysical Research: Solid Earth*, **128**(8), e2023JB026975, e2023JB026975 2023JB026975.
- Rettenberger, S., Meister, O., Bader, M., & Gabriel, A.-A., 2016. ASAGI: a parallel server for adaptive geoinformation, in *Proceedings of the Exascale Applications and Software Conference 2016*, pp. 1–9.
- Rippa, S., 1999. An algorithm for selecting a good value for the parameter  $c$  in radial basis function interpolation, *Advances in Computational Mathematics*, **11**(2/3), 193–210.
- Rodgers, A. J., Pitarka, A., Petersson, N. A., Sjögreen, B., & McCallen, D. B., 2018. Broadband (0–4 Hz) ground motions for a magnitude 7.0 Hayward fault earthquake with three-dimensional structure and topography, *Geophysical Research Letters*, **45**(2), 739–747.
- Rodgers, A. J., Pitarka, A., Pankajakshan, R., Sjögreen, B., & Petersson, N. A., 2020. Regional-scale 3D ground-motion simulations of Mw 7 earthquakes on the Hayward fault, northern California resolving frequencies 0–10 Hz and including site-response corrections, *Bulletin of the Seismological Society of America*, **110**(6), 2862–2881.
- Roten, D., Olsen, K., Day, S., Cui, Y., & Fäh, D., 2014. Expected seismic shaking in Los Angeles reduced by San Andreas fault zone plasticity, *Geophysical Research Letters*, **41**(8), 2769–2777.

- Rubinstein, J. L. & Beroza, G. C., 2004. Evidence for widespread nonlinear strong ground motion in the Mw 6.9 Loma Prieta earthquake, *Bulletin of the Seismological Society of America*, **94**(5), 1595–1608.
- SCEDC, 2013. Southern California Earthquake Data Center.
- Shaw, J. H. & Shearer, P. M., 1999. An elusive blind-thrust fault beneath metropolitan Los Angeles, *Science*, **283**(5407), 1516–1518.
- Shaw, J. H., Plesch, A., Dolan, J. F., Pratt, T. L., & Fiore, P., 2002. Puente hills blind-thrust system, Los Angeles, California, *Bulletin of the Seismological Society of America*, **92**(8), 2946–2960.
- Shaw, J. H., Plesch, A., Tape, C., Suess, M. P., Jordan, T. H., Ely, G., Hauksson, E., Tromp, J., Tanimoto, T., Graves, R., et al., 2015. Unified structural representation of the southern California crust and upper mantle, *Earth and Planetary Science Letters*, **415**, 1–15.
- Shi, Y., Lavrentiadis, G., Asimaki, D., Ross, Z. E., & Azizzadenesheli, K., 2024. Broadband ground-motion synthesis via generative adversarial neural operators: Development and validation, *Bulletin of the Seismological Society of America*, **114**(4), 2151–2171.
- Small, P., Gill, D., Maechling, P. J., Taborda, R., Callaghan, S., Jordan, T. H., Olsen, K. B., Ely, G. P., & Goulet, C., 2017. The SCEC unified community velocity model software framework, *Seismological Research Letters*, **88**(6), 1539–1552.
- Smith, J. D., Azizzadenesheli, K., & Ross, Z. E., 2020. Eikonet: Solving the Eikonal equation with deep neural networks, *IEEE Transactions on Geoscience and Remote Sensing*, **59**(12), 10685–10696.
- Spudich, P. & Chiou, B. S., 2008. Directivity in NGA earthquake ground motions: Analysis using isochrone theory, *Earthquake Spectra*, **24**(1), 279–298.
- Stephenson, W. J., Reitman, N. G., & Angster, S. J., 2017. P-and S-wave velocity models incorporating the Cascadia subduction zone for 3D earthquake ground motion simulations, Version 1.6—Update for Open-File Report 2007–1348, Tech. rep., US Geological Survey.
- Süss, M. P. & Shaw, J. H., 2003. P wave seismic velocity structure derived from sonic logs and industry reflection data in the Los Angeles basin, California, *Journal of Geophysical Research: Solid Earth*, **108**(B3).
- Taborda, R., Azizzadeh-Roodpish, S., Khoshnevis, N., & Cheng, K., 2016. Evaluation of the southern California seismic velocity models through simulation of recorded events, *Geophysical Journal International*, **205**(3), 1342–1364.
- Taufiqurrahman, T., Gabriel, A.-A., Ulrich, T., Valentova, L., & Gallovič, F., 2022. Broadband dynamic rupture modeling with fractal fault roughness, frictional heterogeneity, viscoelasticity and topography: The 2016 Mw 6.2 Amatrice, Italy earthquake, *Geophysical Research Letters*, **49**(22), e2022GL098872.

- Uphoff, C. & Bader, M., 2016. Generating high performance matrix kernels for earthquake simulations with viscoelastic attenuation, in *2016 International Conference on High Performance Computing & Simulation (HPCS)*, pp. 908–916, IEEE.
- Uphoff, C., Rettenberger, S., Bader, M., Madden, E. H., Ulrich, T., Wollherr, S., & Gabriel, A.-A., 2017. Extreme scale multi-physics simulations of the tsunamigenic 2004 Sumatra megathrust earthquake, in *Proceedings of the International Conference for High Performance Computing, Networking, Storage and Analysis, SC '17*, Association for Computing Machinery, New York, NY, USA.
- van Driel, M., Krischer, L., Stähler, S. C., Hosseini, K., & Nissen-Meyer, T., 2015. Instaseis: Instant global seismograms based on a broadband waveform database, *Solid Earth*, **6**(2), 701–717.
- van Driel, M., Boehm, C., Krischer, L., & Afanasiev, M., 2020. Accelerating numerical wave propagation using wavefield adapted meshes. Part I: forward and adjoint modelling, *Geophysical Journal International*, **221**(3), 1580–1590.
- Wang, T., Trugman, D., & Lin, Y., 2021. SeismoGen: Seismic waveform synthesis using GAN with application to seismic data augmentation, *Journal of Geophysical Research: Solid Earth*, **126**(4), e2020JB020077.
- Wang, X. & Zhan, Z., 2020. Moving from 1-D to 3-D velocity model: Automated waveform-based earthquake moment tensor inversion in the Los Angeles region, *Geophysical Journal International*, **220**(1), 218–234.
- Willcox, K. & Peraire, J., 2002. Balanced model reduction via the proper orthogonal decomposition, *AIAA journal*, **40**(11), 2323–2330.
- Withers, K. B., Moschetti, M. P., & Thompson, E. M., 2020. A machine learning approach to developing ground motion models from simulated ground motions, *Geophysical Research Letters*, **47**(6), e2019GL086690.
- Worden, C. B. & Wald, D. J., 2016. ShakeMap 4 Manual — ShakeMap Documentation documentation, <http://usgs.github.io/shakemap/>.
- Xiao, D., Fang, F., Pain, C., & Hu, G., 2015. Non-intrusive reduced-order modelling of the Navier–Stokes equations based on RBF interpolation, *International Journal for Numerical Methods in Fluids*, **79**(11), 580–595.
- Yang, Y., Liu, C., & Langston, C. A., 2020. Processing seismic ambient noise data with the continuous wavelet transform to obtain reliable empirical Green’s functions, *Geophysical Journal International*, **222**(2), 1224–1235.
- Yang, Y., Gao, A. F., Castellanos, J. C., Ross, Z. E., Aizzadenesheli, K., & Clayton, R. W., 2021. Seismic wave propagation and inversion with neural operators, *The Seismic Record*, **1**(3), 126–134.

Yang, Y., Gao, A. F., Azizzadenesheli, K., Clayton, R. W., & Ross, Z. E., 2023. Rapid seismic waveform modeling and inversion with neural operators, *IEEE Transactions on Geoscience and Remote Sensing*, **61**, 1–12.

Zhao, L., Chen, P., & Jordan, T. H., 2006. Strain Green’s tensors, reciprocity, and their applications to seismic source and structure studies, *Bulletin of the Seismological Society of America*, **96**(5), 1753–1763.

Zou, C., Azizzadenesheli, K., Ross, Z. E., & Clayton, R. W., 2023. Deep neural helmholtz operators for 3d elastic wave propagation and inversion, *arXiv preprint arXiv:2311.09608*.

## A Elementary Moment Tensors

The elementary moment tensors are fundamental components used to describe the seismic source mechanism. A seismic source can be expressed as a combination of the six basis tensors  $\widehat{\mathbf{M}}_i$ . The six elementary moment tensors are as follows (Kikuchi & Kanamori, 1991):

$$\begin{aligned} \widehat{\mathbf{M}}_1 &= \begin{bmatrix} 0 & 1 & 0 \\ 1 & 0 & 0 \\ 0 & 0 & 0 \end{bmatrix}, & \widehat{\mathbf{M}}_2 &= \begin{bmatrix} 1 & 0 & 0 \\ 0 & -1 & 0 \\ 0 & 0 & 0 \end{bmatrix}, & \widehat{\mathbf{M}}_3 &= \begin{bmatrix} 0 & 0 & 0 \\ 0 & 0 & 1 \\ 0 & 1 & 0 \end{bmatrix}, \\ \widehat{\mathbf{M}}_4 &= \begin{bmatrix} 0 & 0 & 1 \\ 0 & 0 & 0 \\ 1 & 0 & 0 \end{bmatrix}, & \widehat{\mathbf{M}}_5 &= \begin{bmatrix} -1 & 0 & 0 \\ 0 & 0 & 0 \\ 0 & 0 & 1 \end{bmatrix}, & \widehat{\mathbf{M}}_6 &= \begin{bmatrix} 1 & 0 & 0 \\ 0 & 1 & 0 \\ 0 & 0 & 1 \end{bmatrix}. \end{aligned}$$